

THERMAL TIDES IN SHORT PERIOD EXOPLANETS

PHIL ARRAS¹ AND ARISTOTLE SOCRATES²

Draft version October 25, 2018

ABSTRACT

Time-dependent insolation in a planetary atmosphere induces a mass quadrupole upon which the stellar tidal acceleration can exert a force. This “thermal tide” force can give rise to secular torques on the planet and orbit as well as radial forces causing eccentricity evolution. We apply this idea to the close-in gas giant exoplanets (“hot Jupiters”). The response of radiative atmospheres is computed in a hydrostatic model which treats the insolation as a time-dependent heat source, and solves for thermal radiation using flux-limited diffusion. Fully nonlinear numerical simulations are compared to solutions of the linearized equations, as well as analytic approximations, all of which are in good agreement. We find generically that thermal tide density perturbations *lead* the semi-diurnal forcing. As a result thermal tides can generate asynchronous spin and eccentricity. Applying our calculations to the hot Jupiters, we find the following results: (1) Departure from synchronous spin is significant for hot Jupiters, and increases with orbital period. (2) Ongoing gravitational tidal dissipation in spin equilibrium leads to steady-state internal heating rates up to $\sim 10^{28}$ erg s⁻¹. If deposited sufficiently deep, these heating rates may explain the anomalously large radii of many hot Jupiters in terms of a “tidal main sequence” where cooling balances tidal heating. At fixed stellar type, planet mass and tidal Q , planetary radius increases strongly toward the star inside orbital periods $\lesssim 2$ weeks. (3) There exists a narrow window in orbital period where small eccentricities, e , grow exponentially with a large rate. This window may explain the $\sim 1/4$ of hot Jupiters which should have been circularized by the gravitational tide long ago, but are observed to have significant nonzero e . Conversely, outside this window, the thermal and gravitational tide both act to damp e , complicating the ability to constrain the planet’s tidal Q .

Subject headings: planets – tides

1. INTRODUCTION

A number of puzzles have arisen for the gas giant exoplanets orbiting close to their parent stars, the “hot Jupiters.”

A large fraction of transiting hot Jupiters are observed to have radii far larger than the radius of Jupiter, R_J , implying high temperatures deep in the planetary interior (Burrows et al. 2000). Strong irradiation has been found to have an insulating effect on planets, slowing their cooling and contraction (Burrows et al. 2000). This effect can explain radii $R_p \sim (1.0 - 1.2) \times R_J$, but is insufficient to explain the radii of a significant fraction of the population with $R_p \sim (1.2 - 1.8) \times R_J$ (see Fortney 2008 for a recent review). A powerful internal heat source must be acting to prevent these planets from contracting.

Circularization of the planet’s orbit by dissipation of the gravitational tide has been invoked to explain the small eccentricities of most hot Jupiters (Rasio et al. 1996; Marcy et al. 1997). Using Jupiter’s inferred tidal $Q = 10^5 - 10^6$ (Yoder & Peale 1981), orbits are expected to be circular out to orbital periods $P_{\text{orb}} \lesssim 1$ week. Curiously, a large fraction of the population that *should* have been circularized in \sim Gyrs is not (Dobbs-Dixon et al. 2004; Matsumura et al. 2008). The zero and nonzero eccentricity planets occupy the same orbital period range. Suggested explanations are tidal interaction with

a rapidly rotating young star (Dobbs-Dixon et al. 2004), perturbations from other planets, or a large range of tidal $Q = 10^5 - 10^9$ (Matsumura et al. 2008). In the continued absence of a detectable perturber with appropriate mass and orbit to account for the observed eccentricity, a mechanism involving an isolated star and planet is needed. It is also not clear why planets with presumably similar internal structure and orbits should have such different levels of internal friction.

In the absence of direct observations, it is commonly assumed that the rotation of present day hot Jupiters is highly synchronous. This assumption is motivated by the short (\sim Myr) synchronization time using $Q = 10^5 - 10^6$ for the gas giant. However, despite the short expected synchronization time, hot Jupiters are particularly susceptible to develop asynchronous rotation. Gas giants are relatively frictionless compared to terrestrial planets with $Q \sim 10 - 100$. Even weak opposing external torques may compete with the gravitational tide to produce asynchronous spin.

The proximity of hot Jupiters to their parent star, $\sim 10^2$ times closer than Solar System giants, implies an insolation stronger by $\sim 10^4$ and stellar tidal forces stronger by $\sim 10^6$. Insolation and tidal forces may then play a far more important role for close-in planets. In this paper we discuss “thermal tide torques”, which are created through the interplay of stellar irradiation and gravitational tidal forces.

Gold & Soter (1969) first applied thermal tide torques to explain the observed rotation rate of Venus. A number of more detailed studies followed (e.g. Ingersoll and

Electronic address: arras@virginia.edu, socrates@ias.edu

¹ Department of Astronomy, University of Virginia, P.O. Box 400325, Charlottesville, VA 22904-4325

² Institute for Advanced Study, Einstein Drive, Princeton, NJ 08540

Dobrovolskis 1981). Venus resides in state of slow retrograde rotation. Gravitational tides acting alone would have synchronized Venus’ spin to high precision. Furthermore, Venus’ spin seems to be in resonance with Earth’s orbit. Tides from Earth acting on permanent quadrupole in Venus should have a negligible effect in comparison to solar gravitational torques. The possibility that torques from solar gravitational and thermal tides nearly balance that allows a small effect such as tidal forces from Earth to have an observable effect.

Previous studies of the thermal tide have assumed a thin atmosphere on top of a solid surface, as appropriate for Venus and Earth. In addition, they have assumed that the gravitational tide is strongly dissipative ($Q \sim 10 - 100$). In applying the thermal tide to close-in gas giant planets, a difference between our model and those for Venus and Earth is that we assume an optically thick atmosphere, rather than ground, completely absorbs the stellar radiation. We include flux-limited radiative diffusion of heat above and below this absorbing layer. We find thermal diffusion is crucial in order to accurately estimate the magnitude of the thermal tide, particularly for long forcing periods. In applying our results, we find that the thermal tide can affect not only the planet’s spin, but also the eccentricity and radius for close-in planets.

The plan of the paper is as follows. §2 contains a qualitative discussion of why thermal tide effects are important. There, we argue that spin, eccentricity and global energetics of hot Jupiters are determined by the competition between the thermal and gravitational tides. §3 contains a detailed treatment of atmospheric response to time-dependent insolation, and the resultant quadrupole moments. Readers wishing to ignore these technical details should skip this section. Basic equations and geometry are introduced in §3.1, the heating function is expanded in a Fourier series in §3.2, temperature profiles from the nonlinear simulations are discussed in §3.3, quadrupole moments are computed in §3.4, linear perturbation equations are derived in §3.5, and analytic solutions in the high and low frequency limits are presented in §3.6 and 3.7, respectively. Applications to hot Jupiter spin, radius and eccentricity are in the following sections. Equilibrium spin frequencies are computed in §4. §5 contains tidal heating rates, and a discussion of the energetics required to power the observed radii. §6 contains eccentricity growth/decay rates due to both the thermal and gravitational tides. Our most detailed results for the simultaneous equilibria of spin rate, planetary radius and eccentricity are contained in §7. In §8 we qualitatively discuss how thermal and gravitational tidal forces may drive differential rotation which, in itself, may lead to dissipation. Summary and conclusions are presented in §9. The Appendices contains a derivation of the torque, orbital evolution rates, and tidal heating rates due to the presence of mass quadrupoles of arbitrary form, as well as the mass-radius relation and core luminosity.

2. BASIC IDEA AND INITIAL ESTIMATES

Tidal forces become increasingly important with decreasing orbital radius. Acting alone, dissipation of the gravitational tide leads to synchronous spin and circular orbit for the planet. Thermal tide torques complicate this simple model, leading to qualitatively different evo-

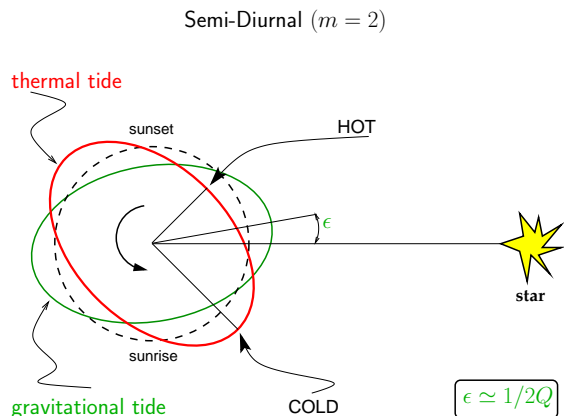


FIG. 1.— Geometry of the semi-diurnal ($m = 2$) thermal and gravitational tidal density perturbations. The planet rotates counterclockwise. In order for the torque to push the planet away from synchronous spin, the density perturbation must *lead* the line joining the planet and star.

lution. A conceptual introduction and order of magnitude estimates are given below.

2.1. Induced Quadrupoles

First we summarize the gravitational tide. The stellar tidal force raises a bulge on the planet, quantified to lowest order by the quadrupole moment

$$Q^{(\text{grav})} \sim \left(\frac{h_t}{R_p} \right) M_p R_p^2 \sim M_\star R_p^2 \left(\frac{R_p}{a} \right)^3. \quad (1)$$

Here R_p and M_p are the radius and mass of the planet, M_\star is the mass of the star, a is the semi-major axis of the orbit, and $h_t \sim R_p (M_\star / M_p) (R_p / a)^3$ is the height of the tide. In the absence of friction within the planet, the gravitational tide does not cause secular evolution of the orbital elements or spin. The presence of friction causes high tide to lag maximum tidal acceleration at noon and midnight. For the case of asynchronous spin, this implies that the tidal bulge is misaligned with the line joining the planet and star, as pictured in figure 1. The stellar tidal force then torques the planet by “pulling” on the projection of the quadrupole moment $Q^{(\text{grav})}$ perpendicular to the star-planet line. This small lag in phase or time is conveniently parametrized by the tidal Q parameter (e.g. Goldreich and Soter 1965). The effective quadrupole moment contributing to secular evolution is

$$Q_{\text{sec}}^{(\text{grav})} \sim \left(\frac{Q^{(\text{grav})}}{Q} \right) \left(\frac{\sigma}{n} \right) \quad (2)$$

where σ is the tidal forcing frequency and n is the orbital frequency. The factor σ/n ensures the misalignment of the tidal bulge vanishes for synchronous and circular orbits (see §3.4). The torque, N , on the planet due to this quadrupole moment scales as $N \sim n^2 Q_{\text{sec}}^{(\text{grav})}$.

Jupiter’s Q is thought to be in the range $Q = 10^5 - 10^6$ based on expansion of Io’s orbit to form the Laplace resonance (e.g. Yoder & Peale 1981). Several studies have also found that hot Jupiters should have $Q = 10^5 - 10^6$ to explain the circularization of their orbits on Gyr timescales (e.g. Ogilvie & Lin 2004; Wu 2005). These studies assume that the gravitational tide is acting alone. Here, we show that constraints on Q of extrasolar planets are complicated by the influence of the thermal tide.

Another possibility for tidal phenomena comes from intense time-dependent insolation. Time-dependence may arise either through asynchronous rotation or orbital eccentricity. For circular orbits and asynchronous spin, the diurnal forcing frequency is $\sigma = n - \Omega$, where Ω is the planet’s spin frequency. There is also power at the higher harmonics $\sigma = m(n - \Omega)$, where m is the azimuthal wavenumber. Since the diurnal component does not generate a quadrupole moment which can couple to the stellar tidal field, the semi-diurnal component ($m = 2$) dominates the torque on the planet. The magnitude of the thermal tide quadrupole is roughly (see §3.6 and 3.7)

$$Q^{(\text{th})} \sim \frac{\Delta M R_p^2}{(\sigma t_{\text{th}})^\delta} \quad (3)$$

where ΔM is the mass of the atmospheric layer heated by time-dependent insolation,

$$t_{\text{th}} \sim \frac{\Delta M C_p T}{R_p^2 F_\star}, \quad (4)$$

the exponent $\delta \sim 0.5 - 1.0$ and F_\star is the flux at the sub-stellar point. The thermal time, t_{th} , is the time required for the layer of mass ΔM to absorb/emit its thermal energy.

One of our principal goals is to show that for the atmospheres of interest, the thermal tide bulge leads the sub-stellar point, opposite the behavior of the dissipative gravitational tide. Ingersoll & Dobrovolskis (1978) made similar arguments for Venus based on two assumptions. First, the temperature of the absorbing layer lags the time of maximum heating, similar to our daily experience on Earth. Second, that fluid elements remain at roughly constant pressure. Regions of lower temperature then imply higher density and vice versa, and the high density regions (“tidal bulges”) lead the sub-stellar point. In our analysis, we adopt this simplifying “constant pressure approximation.” The horizontal readjustment of mass necessarily requires zonal winds. In this paper we do not solve for the wind structure; see Dobrovolskis & Ingersoll (1980) for the wind structure resulting from a similar calculation applied to Venus.

Both the gravitational and thermal tidal bulges can be torqued by the stellar tidal field. The angular momentum evolves due to the net torque. In spin equilibrium, the thermal and gravitational tide torques balance, in general leading to an asynchronous spin state. We estimate the ratio of quadrupole moments to be (eq.2 and 3)

$$\begin{aligned} \frac{Q^{(\text{th})}}{Q_{\text{sec}}^{(\text{grav})}} &\sim \left(\frac{n}{\sigma}\right)^{1+\delta} \left(\frac{\Delta M a^3}{M_\star R_p^3}\right) \left(\frac{Q}{(nt_{\text{th}})^\delta}\right) \\ &\simeq \left(\frac{n}{\sigma}\right)^{1+\delta} \left(\frac{\Delta M}{10^{-8} M_p}\right) \left(\frac{M_p}{10^{-3} M_\star}\right) \\ &\times \left(\frac{a}{100 R_p}\right)^3 \left(\frac{Q}{10^5}\right) \frac{1}{(nt_{\text{th}})^\delta}. \end{aligned} \quad (5)$$

This order of magnitude estimate shows that for parameters characteristic of the hot Jupiters the thermal and gravitational tide effects can be comparable. Setting eq.5 equal to unity allows one to estimate the equilibrium spin frequency since $\sigma \propto n - \Omega$.

2.2. Orbit, spin, and thermal equilibrium

Gravitational tidal dissipation converts rotational and orbital energy into heat. When the gravitational tide alone acts, the end state is synchronous spin and a circular orbit. As torque equilibrium is realized in \sim Myr, over Gyr timescales the only source of tidal heating is finite eccentricity. In the absence of an external perturbation continually pumping the eccentricity, tidal heating is limited by the initial energy reservoir in the orbit $\sim GM_\star M_p e^2 / 2a$, which may be comparable to planet’s binding energy for initially eccentric orbits (Bodenheimer et al. 2001).

Planets with anomalously large radii but small eccentricity, such as HD 209458b with $e \simeq 0.01$ (Laughlin et al. 2005), are difficult to explain with the gravitational tide alone since the current eccentricity implies negligible tidal heating. In order to explain the large radius with transient tidal heating one has to invoke that heating ended recently, and we are observing the planet before it has had time to contract. Since contraction times for radii $(1.2 - 1.8) \times R_J$ are much shorter than a Gyr, this argument requires that we observe these systems during a special time in their evolution.

Inclusion of the thermal tide qualitatively changes this picture. A steady state may be reached in which thermal and gravitational tide effects balance one another. In this scenario, gravitational tidal dissipation continues to act in the equilibrium state, due to asynchronous spin and/or eccentricity. The thermal tide forces are not inherently dissipative. However differential rotation set up in the atmosphere by opposing torques at different depths may cause significant heating.

Tangential forces applied to the thermal tide quadrupole torque the planet away from synchronous spin. In equilibrium, the thermal and gravitational tide torques on the planet are in balance, setting the equilibrium spin rate. The timescale to attain equilibrium spin is shorter than the Gyrs age for orbital periods up to several months. Radial forces from the thermal tide quadrupole act to alter the orbital eccentricity. If both the thermal and gravitational tides act to circularize the orbit, the equilibrium state is again zero eccentricity. However, the thermal tide can also pump eccentricity, opposing the gravitational tide. In that case, a balance of thermal and gravitational tides implies nonzero values for the equilibrium eccentricity. The timescale to attain equilibrium eccentricity is shorter than the age for planets with orbital periods shorter than ~ 1 week. Lastly, in the absence of tidal heating, planets cool and contract. If tides deposit heat deep in the convective interior of the planet, a thermal equilibrium is possible in which heating of the core is balanced by outward heat loss at the radiative-convective boundary. We find thermal equilibrium is achieved on a timescale shorter than the age for orbital periods $\lesssim 1$ week (see section 7).

The thermal tide torque is exerted on a layer near the photosphere of the stellar radiation. The depth dependence of the gravitational tide torque is uncertain as the nature of gravitational tidal dissipation is complicated and not yet fully understood. For instance, turbulent viscosity damping would mainly occur just below the radiative-convective boundary (Goldreich & Nicholson 1977; Wu 2005), shear layers due to “wave attractors”

reside deep in the convective core (Ogilvie & Lin 2004; Goodman & Lackner 2008), and upward propagating waves generated at the tropopause may break above the photosphere (Ogilvie & Lin 2004). If the thermal and gravitational torques are not exerted at the same depth, differential rotation is induced, distinct from the usual thermally-driven circulation patterns. For simplicity, we defer effects due to differential rotation until §8.

2.3. Energetics, and implications for the lightcurve and spectrum

The stellar tidal acceleration creates regions of high and low gravitational potential in the longitudinal direction. Insolation heats the fluid, and this heat can be tapped to perform work against the stellar tidal field by causing pressure gradients which move fluid from regions of low to high potential. The ultimate source of energy for tidal heating driven by the thermal tide is then the stellar radiation field. The rate of work done by the thermal tide is

$$\dot{E}_{\text{work}}^{(\text{TT})} \simeq -\Delta M \frac{\sigma}{m} \oint (-\nabla U) \cdot d\mathbf{l} \simeq -\frac{\sigma}{m} N^{(\text{TT})}, \quad (6)$$

where U is the tidal potential, $\sigma = 2(n - \Omega)$, $m = 2$, and the integral is taken along a fluid trajectory $d\mathbf{l} = R_p d\phi \hat{\phi}$. Here $N^{(\text{TT})} \simeq \Delta M \oint (-\nabla U) \cdot d\mathbf{l}$ is the thermal tide torque on the heated layer. In torque equilibrium, the thermal and gravitational tide torques balance giving $N^{(\text{GT})} = -N^{(\text{TT})}$. The heating rate due to the gravitational tide is then

$$\dot{E}_{\text{heat}}^{(\text{GT})} = \frac{\sigma}{m} N^{(\text{GT})} = -\frac{\sigma}{m} N^{(\text{TT})} = \dot{E}_{\text{work}}^{(\text{TT})}, \quad (7)$$

showing explicitly that the work done on the atmosphere by the thermal tide is converted into heat by the gravitational tide in steady state.

Since the work done on the atmosphere is ultimately powered by the stellar radiation, the maximum power input is given by the rate of absorption of stellar flux,

$$\begin{aligned} \dot{E}_{\text{max}} &= L_{\star} \left(\frac{R_p}{2a} \right)^2 (1 - e^2)^{-1/2} \\ &= 9 \times 10^{28} \text{ erg s}^{-1} \left(\frac{R_p}{R_J} \right)^2 \left(\frac{L_{\star}}{L_{\odot}} \right) \\ &\quad \times \left(\frac{M_{\odot}}{M_{\star}} \right)^{2/3} \left(\frac{4 \text{ days}}{P_{\text{orb}}} \right)^{4/3} (1 - e^2)^{-1/2} \end{aligned} \quad (8)$$

where L_{\star} is the stellar luminosity and $P_{\text{orb}} = 2\pi/n$ is the orbital period. We will show in §5 that the efficiency of converting stellar flux to heat by gravitational tidal dissipation is as high as $\sim 1 - 10\%$, and increases toward the star.

Some of the heat deposited by insolation is converted into work, leading to less thermal energy immediately re-radiated back out into space. In the (unphysical) limit of 100% efficient conversion of heat to work, and no subsequent conversion of kinetic energy back into heat, the atmosphere would be far cooler than the equilibrium temperature, and the thermal emission from the planet would be solely due to the flux coming out from the core. In torque equilibrium, the work done on the atmosphere

by the thermal tide is converted into heat by the gravitational tide. We presume the gravitational tide dissipation occurs in the convective core, and entropy is efficiently mixed throughout. The temperature profile as a function of depth, latitude and longitude may then differ markedly from the case with no tidal heating.

First consider the change in the lightcurve for thermal radiation. For small flux from the core, and short thermal time in the absorbing layer, there will be a large day-night temperature difference. If, for example, 1% of the insolation is deposited in the core by the gravitational tide, then the day-night temperature ratio is $(F_{\text{core}}/F_{\star})^{1/4} \sim 0.01^{1/4} \sim 0.3$, where F_{core} is the flux emerging from the convective core. For small F_{core} , the only possibility of high temperature on the night side is redistribution of heat by zonal winds. Tidal dissipation generating a large F_{core} provides an alternative means to reduce the day-night temperature contrast (see figure 11 for the luminosity exiting the core versus planetary radius).

A change in the vertical distribution of heat sources also affects the vertical temperature profile at the depths where the spectrum is formed. Depositing heat in the core rather than at the photosphere leads to a radiative flux more constant with depth near the photosphere. This alteration of the temperature profile may in principle be imprinted on the spectrum.

3. TEMPERATURE PROFILES AND QUADRUPOLE MOMENTS

In this section we describe the model for time-dependent thermal forcing of hot Jupiter atmospheres due to asynchronous rotation and/or an eccentric orbit, as well as the resultant gravitational forces on the perturbed atmosphere. The full nonlinear equations are presented, and then approximated as a time-independent background and harmonic perturbations. Analytic solutions are developed for the background and perturbations, and compared to the full nonlinear solutions.

3.1. Equations and geometry

We consider a planet and star of mass and radius (M_p, R_p) and (M_{\star}, R_{\star}) , respectively. The planet orbits with separation $D(t)$ and true anomaly $\Phi(t)$ which we will treat as a nearly Keplerian orbit with semi-major axis a , eccentricity e and mean motion $n = [G(M_{\star} + M_p)/a^3]^{1/2}$. We consider an atmosphere in uniform rotation with rate Ω , and the spin and orbital angular momentum aligned. Differential rotation will be discussed in §8. We will work in a non-rotating coordinate system whose origin is at the center of the planet, and whose axes are fixed with respect to distant observers. Spherical polar coordinates (θ, ϕ) are used, where the star orbits at the equator with a colatitude $\theta = \pi/2$ and longitude $\phi = \Phi(t)$, and a fixed point on the planet rotates with angular frequency $\dot{\phi} = \Omega$. The derivative comoving with the planet is then $d/dt = \partial/\partial t + \Omega\partial/\partial\phi$. The cosine of the angle χ between the vertical and the vector to the star is $\cos \chi = \sin \theta \cos(\phi - \Phi)$. The day side is over the angular range $-\pi/2 \leq \phi - \Phi \leq \pi/2$. Let z be the altitude above some appropriate reference level and $y(z) = \int_z^{\infty} dz' \rho(z')$ the mass column above that altitude. The atmosphere is treated as being both thin and in hydrostatic balance,

hence the pressure $P = gy$, where the surface gravity is $g = GM_p/R_p^2$.

We use an approximate treatment of radiative transport in which the time-dependent insolation is treated as a specified heat source. We approximate the transfer of thermal radiation by flux-limited diffusion. For the thermal radiation, we employ the solar composition “condensed” phase Rosseland opacities of Allard et al. (2001), which include the effect of grains in the equation of state, but ignores their opacity, as is appropriate if the grains have rained out to higher depth. There is a prominent dip in κ along isobars centered around $T = 2000$ K. This feature will be apparent in our numerical results.

We use the equation of state from Saumon et al. (1995), with 70% hydrogen and 30% helium by mass. At low density, this is an ideal gas equation of state $P = \rho k_b T / \mu m_p$, where ρ is the mass density, T is the temperature, m_p is the proton mass, k_b is Boltzmann’s constant, and $\mu \simeq 2.4$ is the mean molecular weight for a mixture of molecular hydrogen and helium.

The temperature and flux are found by solution of the heat equation

$$C_p \frac{dT}{dt} = \frac{\partial F}{\partial y} + \epsilon \quad (9)$$

and the equation for flux-limited diffusion

$$F = \frac{16\sigma_{\text{sb}}T^3\Lambda}{\kappa} \frac{\partial T}{\partial y}. \quad (10)$$

Here $C_p \simeq 7k_b/2\mu m_p$ is the specific heat per gram, and ϵ is the heating rate per gram. Since column, or equivalently pressure, is assumed constant for fluid elements, the thermodynamic relation $ds/C_p = dT/T - \nabla_{\text{ad}}dP/P$ is simplified to $Tds = C_p dT$. We ignore vertical fluid motion relative to constant pressure surfaces, as well as horizontal motions relative to the mean rate Ω . The quantity Λ is the flux limiter, which allows a smooth transition between the optically thick regime, $\Lambda = 1/3$, and the optically thin regime $\Lambda \rightarrow 0$. For convenience, we use the limiter prescription of Levermore & Pomraning (1981)

$$\Lambda = \frac{2 + R}{6 + 3R + R^2} \quad (11)$$

where $R = (4/\kappa)|\partial \ln T / \partial y|$ is the ratio of photon mean free path to temperature scale height. The boundary conditions are (1) the radiation free streams at small optical depths, $F \simeq 4\sigma_{\text{sb}}T^4$, and (2) $F \rightarrow F_{\text{core}}$ at large y , where F_{core} is the thermal flux that emerges from the convective core.

We refer to direct solutions of eq.9 and 10 as “nonlinear solutions”, as temperature changes are not assumed to be small. The nonlinear solutions will be compared to solutions of the linearized equations which are valid only for small temperature changes.

To numerically solve eq.9 and 10, we adapted the code of Piro et al. (2005). We use second-order finite difference in y and backward difference in t for stability. Typically 128 y grid points were used, but selected results were checked at higher resolution and found to be accurate. The time step is set so that the average temperature at each grid point changes by $\lesssim 10^{-3}$ over the time step.

A background model, which we discuss below, is used as an initial condition, and the initial time taken to be noon ($\phi = \Phi$). Transients due to the initial conditions are observed to relax over a few forcing periods.

3.2. Time-dependent insolation and Fourier components

The time-dependent heating rate per unit mass is given by Beer’s Law (Liou 2002)

$$\epsilon(y, \theta, \phi, t) = \kappa_* F_*(D) \exp\left(-\frac{\kappa_* y}{\cos \chi}\right) \Theta(\cos \chi) \quad (12)$$

where the constant κ_* specifies the column ($y \sim \kappa_*^{-1}$) at which the stellar radiation is absorbed, and $F_*(D) = \sigma_{\text{sb}}T_*^4(R_*/D)^2$ is the bolometric stellar flux at the sub-solar point on the planet. We present numerical results only for a solar-like star with $M_* = M_\odot$, $T_* = 5780$ K and $R_* = R_\odot$. However, our analytic analysis allows for rescaling to stars of different mass and luminosity. The step function $\Theta(\cos \chi)$ enforces heating only on the day side. In radiative equilibrium, the thermal flux exiting the top of the atmosphere is

$$F(y = 0, \theta, \phi, t) = F_{\text{core}} + \int_0^\infty dy \epsilon(y, \theta, \phi, t) \\ = F_{\text{core}} + \cos \chi F_* \Theta(\cos \chi). \quad (13)$$

We take the upper limit of integration to be $y = \infty$ since $y = \kappa_*^{-1}$ is a shallow layer in the atmosphere, and the integral converges exponentially.

The gravitational tide can only couple to fluid perturbations with quadrupolar angular dependence and a specific harmonic time dependence. Therefore, we now expand the insolation in terms of a Fourier series in longitude and time. Since $\cos \chi$ depends on only the combination of longitudes $\psi = \phi - \Phi$, we write

$$\epsilon(y, \theta, \phi, t) = \kappa_* F_*(D) \sum_{m=-\infty}^{\infty} g_m \left(\frac{\kappa_* y}{\sin \theta}\right) e^{im(\phi - \Phi)} \quad (14)$$

where the integral

$$g_m(s) \equiv \frac{1}{2\pi} \int_{-\pi/2}^{\pi/2} d\psi e^{-im\psi - s \sec \psi} \quad (15)$$

contains a contribution only from the day side. We compute the integrals $g_m(s)$ numerically. The $m = 0$ term is the average over longitude. For eccentric orbits, using $F_*(D) = F_*(a)(a/D)^2$, the time-dependence can be expanded as a sum of harmonic terms using the Hansen coefficients defined in eq.A13 of appendix A

$$\left(\frac{a}{D}\right)^2 e^{-im\Phi} = \sum_{k=-\infty}^{\infty} X_k^{1m}(e) e^{-iknt}. \quad (16)$$

The heating rate in eq.12 can then be written in a Fourier series in both longitude and time as

$$\epsilon(y, \theta, \phi, t) = \kappa_* F_*(a) \sum_{mk} X_k^{1m}(e) g_m \left(\frac{\kappa_* y}{\sin \theta}\right) e^{im\phi - iknt} \quad (17)$$

The (m, k) ’th term in the series has a forcing frequency $\sigma_{mk} = kn - m\Omega$ in the co-rotating frame and kn in the

inertial frame. The $(m, k) = (0, 0)$ term is the time and longitude averaged heating rate, which we denote as

$$\epsilon(y, \theta) = F_\star(a) \kappa_\star X_0^{10}(e) g_0(\kappa_\star y / \sin \theta). \quad (18)$$

Since $X_0^{1m}(e) = \delta_{m0}(1 - e^2)^{-1/2}$, there are no time-independent ($k = 0$) non-axisymmetric ($m \neq 0$) heating terms. Axisymmetric ($m = 0$) time-dependent heating does occur for eccentric orbits, due to the radial force. For the time-independent background, $\int_0^\infty dx g_0(x) = 1/\pi$ leads to a background surface flux

$$\begin{aligned} F(y = 0, \theta) &= F_{\text{core}} + \int_0^\infty dy \epsilon(y, \theta) \\ &= F_{\text{core}} + \frac{1}{\pi} F_\star(a) X_0^{10}(e) \sin \theta \end{aligned} \quad (19)$$

and thermal luminosity

$$\begin{aligned} L &= R_p^2 \int d\Omega F(y = 0, \theta) \\ &= 4\pi R_p^2 \left(F_{\text{core}} + \frac{X_0^{10}(e)}{4} F_\star(a) \right) \end{aligned} \quad (20)$$

in thermal radiation from the planet. We will use eq.18 to define background models, on top of which we solve for perturbations. We define the time-dependent perturbation to the heating rate as

$$\delta\epsilon(y, \theta, \phi, t) = \kappa_\star F_\star(a) \sum_{m, k \neq 0} X_k^{1m}(e) g_m \left(\frac{\kappa_\star y}{\sin \theta} \right) e^{im\phi - ik\omega t} \quad (21)$$

For $e = 0$, $X_k^{\ell m}(0) = \delta_{mk}$ enforces $k = m$, and the forcing frequency becomes $\sigma_{mm} = m(n - \Omega)$, where $2\pi/|n - \Omega|$ is the diurnal forcing period.

The values of $g_m(s)$ in the heating function decrease with increasing m . While the diurnal ($m = \pm 1$) terms dominate the observable flux variation, they do not contribute to the torque since the tidal potential has no dipole component. The quadrupole moments responsible for spin and orbital evolution are dominated by the semi-diurnal ($m = 0, \pm 2$) components.

3.3. Discussion of temperature profiles

Figures 2 and 3 show temperature versus pressure over one diurnal forcing period for a planet in circular orbit around a solar-type star. The orbital period is $P_{\text{orb}} = 4$ days and the spin period $P_{\text{spin}} = 3$ days, giving a diurnal forcing period of 12 days. Each curve is labeled by phase in the heating cycle, where noon means heating is maximum, etc. Figure 2 illustrates a heating function which extends “deep”, down to a base pressure $P_{\text{base}} = g/\kappa_\star = 10^{5.5}$ dyne cm^{-2} , while figure 3 shows “shallow” heating down to $P_{\text{base}} = g/\kappa_\star = 10^{3.5}$ dyne cm^{-2} . Naively one may have expected the temperature to change significantly only above P_{base} . This is approximately true for the deep heating case. The shallow heating case, however, shows large temperature perturbations extending a factor of ~ 30 deeper in pressure than P_{base} . Heating below P_{base} is due to diffusion, rather than direct absorption of stellar radiation. We will show that there are two limits for the forcing period. In the “high frequency limit”, appropriate for planets at large separation from the star, the temperature perturbations are large only for depths $P \lesssim P_{\text{base}}$. In the “low

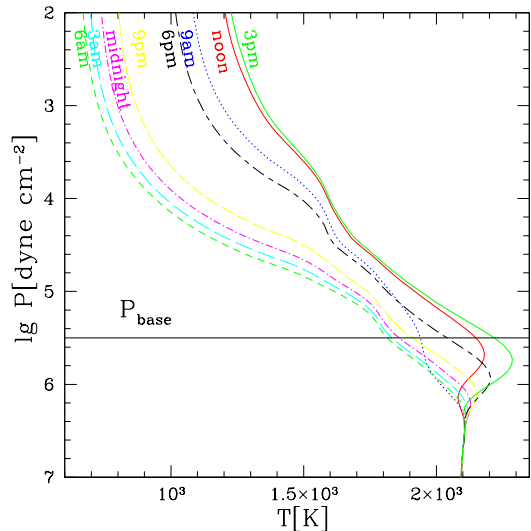


FIG. 2.— Temperature versus pressure over one diurnal forcing period for “deep” forcing at the equator ($\theta = \pi/2$). Note the lag between maximum forcing (at noon) and maximum temperature (between noon and 3pm), and also the pronounced “bump” near the base of the heated layer at $P_{\text{base}} = g/\kappa_\star = 10^{5.5}$ dyne cm^{-2} . This plot was produced using the nonlinear simulations for a circular orbit with $P_{\text{orb}} = 4$ days, super-synchronous rotation $P_{\text{spin}} = 3$ days, $\kappa_\star = 10^{-2.5}$ $\text{cm}^2 \text{g}^{-1}$, $g = 10^3$ cm s^{-2} , $F_{\text{core}} = 10^4$ $\text{erg cm}^{-2} \text{s}^{-1}$ and a solar type star. Noon is the time of maximum heating.

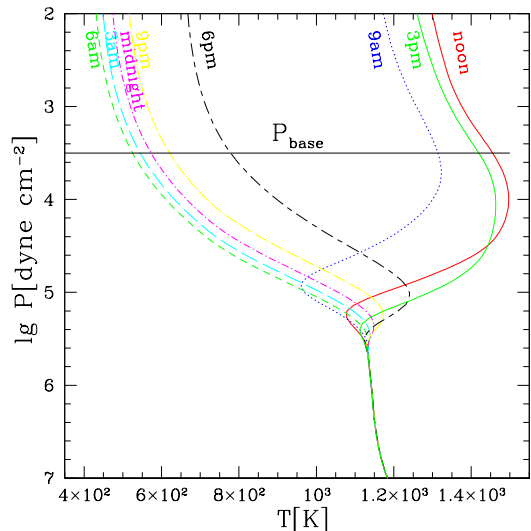


FIG. 3.— Same as figure 2 but with “shallow” forcing $\kappa_\star = 10^{-0.5}$ $\text{cm}^2 \text{g}^{-1}$. The base of the heated layer is now at $P_{\text{base}} = g/\kappa_\star = 10^{3.5}$ dyne cm^{-2} . The temperature perturbations diffuse significantly below the base of the layer directly heated. Here the forcing period, $2\pi/\sigma$, is large in comparison to the thermal time t_{th} at $y \lesssim \kappa_\star^{-1}$ giving temperature maximum in phase with the maximum heating at noon. A thermal diffusion wave penetrates to large depths, and lags in phase with respect to the temperature at $y \lesssim \kappa_\star^{-1}$. This lag in phase leads to a torque that attempts to increase the spin of the planet.

frequency limit”, appropriate for close-in planets, temperature perturbations have time to diffuse down below P_{base} , so that the star torques a layer deeper than that directly heated by the stellar radiation.

The “bump” in the temperature profiles in figure 2 at $P = 10^{5.0} - 10^{6.2}$ dyne cm^{-2} is evidence of an inwardly

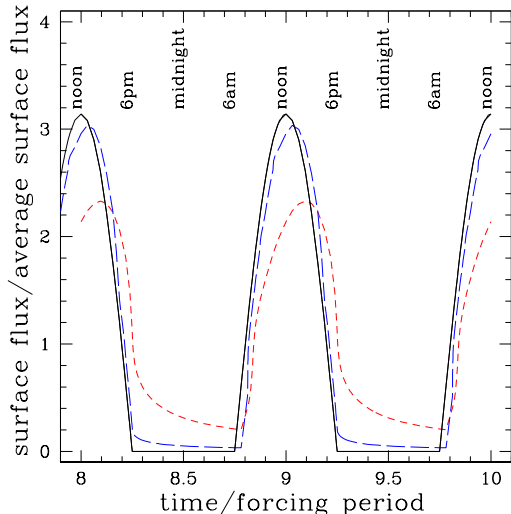


FIG. 4.— Thermal flux at the surface versus time for the cases shown in figures 2 and 3. These simulations are at the equator ($\theta = \pi/2$), flux is normalized by the average surface flux $F_{\text{core}} + F_{\star}(a)/4$, and time is in units of diurnal forcing period (12 days). The solid black line is the outgoing flux if no net heat is absorbed or emitted by the atmosphere (eq.13). The blue long-dashed line is the shallow heating case (figure 3). The red short-dashed line is the deep heating case (figure 2).

propagating thermal diffusion wave. This bump is also seen in temperature profiles in figure 5 of Showman et al. (2008), although the authors do not identify this feature as such. Showman et al. (2008) have a far more detailed solution method, including nonlinear three-dimensional hydrodynamics, angle and frequency dependent radiative transfer, and detailed chemical abundances and monochromatic opacities. That our solutions are in qualitative and rough quantitative agreement in the region of interest lends confidence to our results.

Another important comparison to the more rigorous results of Showman et al. (2008) concerns the lag in the temperature profile, shown in their figure 3. Although their simulation is of a synchronous planet, they generate a super-rotating equatorial jet which mimics the super-synchronous rotation in our results. Those authors indeed find the temperature reaches a maximum *eastward* of the subsolar point; maximum temperature lags maximum heating. This lag is especially prominent at large depth (their bottom panel). We regard this as strong evidence that, while inclusion of fluid motion may alter our results quantitatively, the qualitative result that temperature lags, due to thermal inertia, is in agreement with Showman et al. (2008). A crucial omission in their simulations is that the tidal force from the star is not included. We argue, based on the temperature lag seen in their figure 3, that the torque on this thermally-generated quadrupole will act to generate asynchronous spin.

Figure 4 shows the thermal flux exiting the surface, in units of the average thermal flux, for the two cases shown in figures 2 and 3. The shallow heating case shows larger flux variations and smaller lag time in comparison to the deep heating case. In both cases, the maximum in thermal emission *lags* the maximum in heating (at noon) due to thermal inertia. The Spitzer lightcurves for

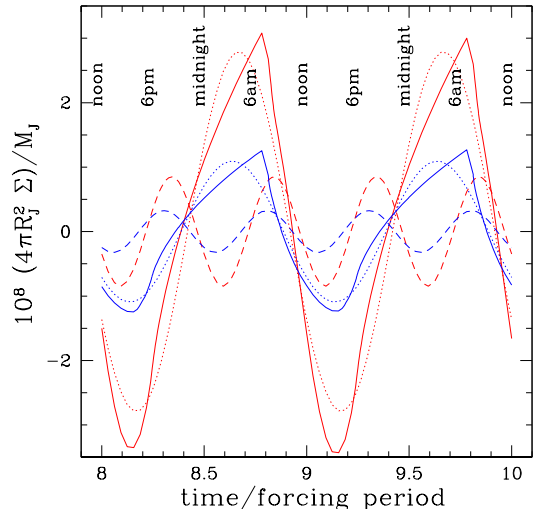


FIG. 5.— Effective column Σ (eq.24), converted into units of fractional mass of the planet, for the deep heating case (red, figure 2) and the shallow heating case (blue, figure 3). The solid lines are the full numerical result. Fourier transform of the solid lines gives the diurnal component (dotted lines) and the semi-diurnal component (dashed lines).

HD 189733b show maximum thermal emission just before secondary eclipse. Using the geometry from figure 1, maximum emission occurs just before secondary eclipse for a planet with *super-synchronous* rotation, in order that the temperature reaches maximum to the *east* of the subsolar point, after it has passed through noon. A similar effect would occur for a super-synchronous zonal wind, as in the model of Showman et al. (2008).

One technical point about flux-limited diffusion is that it produces temperature profiles which increase inward at small optical depth. The “greenhouse” case shown in figure 2 is captured in our solutions. Recall that greenhouse heating is due to $\kappa_{\star} \ll \kappa$; stellar irradiation deposits heat at large optical depth, leading to a temperature increase by a factor $\sim (\kappa/\kappa_{\star})^{1/4}$ above the skin temperature $(F_{\star}/4\sigma_{\text{sb}})^{1/4}$. There has been recent interest in shallow heating, $\kappa_{\star} \gg \kappa$, due to TiO/VO absorption at $P \sim \text{mbar}$, producing an inwardly decreasing temperature profile, the “stratosphere” case (Hubeny et al. 2003; Fortney et al. 2008). To model this effect would require angle and frequency-dependent solution of the transfer equations, beyond the scope of this paper. We note, however, that below P_{base} , the stratosphere case is expected to have temperature $\sim (F_{\star}/\sigma_{\text{sb}})^{1/4}$, similar to our results with flux-limited diffusion. Since the torque is applied well below P_{base} , we expect our results to be qualitatively, and perhaps quantitatively correct.

3.4. Quadrupole moments

Appendix A contains a derivation of the secular changes in e , a and Ω due to a quadrupole moment. In addition, we derive the change in total spin plus orbital energy due to this quadrupole moment. Here, we outline the method of computation for the thermal tide quadrupole moment, as well as review Darwin’s theory of secular evolution for gravitational tides.

The “thermal tide” force results from the mass multiple moments induced in the atmosphere by time-

dependent insolation. The multipole moments are defined in terms of the density field that is the solution to eqs. 9 and 10. We have

$$\mathcal{Q}_{\ell m}^{(\text{TT})}(t) = \int d^3x \rho(\mathbf{x}, t) r^\ell Y_{\ell m}^*(\theta, \phi). \quad (22)$$

The density $\rho(\mathbf{x}, t)$ is computed from the temperature profile $T(\mathbf{x}, t)$ using the ideal gas law and hydrostatic balance $P = gy$. Since $r^\ell \rho(\mathbf{x}, t)$ is a real quantity, and $Y_{\ell m}^* = (-1)^m Y_{\ell, -m}$, the moments must satisfy $(\mathcal{Q}_{\ell m}^{(\text{TT})})^* = \mathcal{Q}_{\ell, -m}^{(\text{TT})}(-1)^m$. As the static and azimuthally symmetric background model has zero quadrupole moment, it can be subtracted off the integrand. We then make a change of integration variable from radius r to column $dy = -\rho dr$, and approximate $r \simeq R_p$, yielding the expression

$$\begin{aligned} \mathcal{Q}_{\ell m}^{(\text{TT})}(t) &= R_p^{2+\ell} \int d\Omega Y_{\ell m}^*(\theta, \phi) \\ &\times \int_0^\infty dy \left(\frac{\rho(\mathbf{x}, t) - \rho(y, \theta)}{\rho(y, \theta)} \right). \end{aligned} \quad (23)$$

Inspection of eq.23 shows that the tide couples to an “effective column”

$$\Sigma(\theta, \phi, t) \equiv \int_0^\infty dy \left(\frac{\rho(\mathbf{x}, t) - \rho(y, \theta)}{\rho(y, \theta)} \right). \quad (24)$$

Figure 5 shows numerical examples of the time-dependent column Σ for the same simulations as in figures 2 and 3. The effective column (solid lines) in general leads the heating function, a consequence of the temperature lag and the constant pressure assumption. We have taken a Fourier transform of the time-series for Σ , and show the diurnal and semi-diurnal components, which also lead. The diurnal component dominates the temperature and density response, but produces no torque since the tidal force has no $\ell = 2$, $m = \pm 1$ components. The semi-diurnal response is smaller, by a factor ~ 2 in the present example, but dominates the torque.

The expressions for the secular change in the planet’s orbit require the Fourier transform in time of the quadrupole moments, which we perform numerically from our simulation output. We define the desired transforms

$$\mathcal{Q}_{\ell m}^{(\text{TT})}(t) \equiv \sum_{m=-\infty}^{\infty} \mathcal{Q}_{\ell m k}^{(\text{TT})} e^{-iknt} \quad (25)$$

where

$$\mathcal{Q}_{\ell m k}^{(\text{TT})} = \frac{n}{2\pi} \int_0^{2\pi/n} dt e^{iknt} \mathcal{Q}_{\ell m}^{(\text{TT})}(t), \quad (26)$$

and satisfy $\mathcal{Q}_{\ell, -m, -k}^{(\text{TT})} = (-1)^m (\mathcal{Q}_{\ell m k}^{(\text{TT})})^*$. For the non-linear simulations, we evolved the atmosphere for 10 forcing periods, and computed the Fourier transforms numerically using orbits 9 and 10.

We now turn to the gravitational tide. The stellar gravitational tidal acceleration $-\nabla U$ induces fluid flow in the planet. Dissipation causes a phase lag $\sim 1/Q$ between the acceleration and high tide, where Q is the tidal quality factor. This phase lag is the origin of the “gravitational tide torque”, which attempts to make the planet’s

spin synchronous. Hut (1981) contains a clear review of Darwin’s theory of tidal evolution. There it is assumed that the fluid response lags forcing by a time τ_{lag} . The quadrupolar fluid response can be viewed as two point masses each of mass $(k_p/2)M_\star [R_p/D(t-\tau_{\text{lag}})]^3$, with longitude $\Phi(t-\tau_{\text{lag}}) - \Omega(t-\tau_{\text{lag}})$ and $\Phi(t-\tau_{\text{lag}}) - \Omega(t-\tau_{\text{lag}}) + \pi$. Here k_p is the apsidal motion constant of the planet, which takes into account the internal structure in the external potential perturbation produced by the quadrupole moment. Under the assumption that τ_{lag} is small in comparison to the forcing period, we expand to first order in τ_{lag} . We ignore the term independent of τ_{lag} as it is in phase with the stellar gravitational tidal forcing and therefore, cannot lead to a torque. We find the effective gravitational tidal quadrupole moment

$$\begin{aligned} \mathcal{Q}_{2m}^{(\text{GT})}(t) &= i\tau_{\text{lag}} k_p M_\star R_p^2 Y_{2m}(\pi/2, 0) \left(\frac{R_p}{a} \right)^3 \\ &\times \sum_k (kn - m\Omega) X_k^{2m}(e) e^{-iknt}, \end{aligned} \quad (27)$$

which is defined in the inertial frame. Rewriting this expression in terms of $Q'_p = (3/2k_p)(1/n\tau_{\text{lag}})$ (Mardling & Lin 2002) and by taking the Fourier transform in time, we find the imaginary component

$$\begin{aligned} \text{Im} \left(\mathcal{Q}_{2mk}^{(\text{GT})} \right) &= \left(\frac{3}{2Q'_p} \right) \left(\frac{M_\star R_p^5}{a^3} \right) \left(\frac{kn - m\Omega}{n} \right) \\ &\times Y_{2m}(\pi/2, 0) X_k^{2m}(e). \end{aligned} \quad (28)$$

As a check of this result, we compared eq.28, A16, A17 and A18 against Hut’s analytic formulas for a range of orbital period, spin period and eccentricity.

Note that Hut’s “constant time lag” prescription for orbit and spin evolution disagrees with the “constant lag angle” approach of Goldreich & Soter (1966). The use of a constant lag angle, with a constant Q , is unphysical as the torque is discontinuous as the spin changes from sub- to super-synchronous and vice-versa. By adopting the lag in time approach of Hut (1981) or Mardling & Lin (2002) with the above choice for Q , we find agreement with the results of Goldreich & Soter (1966) when the planet is far from a synchronous spin state, as in the case of the Jupiter-Io system. Therefore, the constraints on Q inferred by Goldreich & Soter (1966) may still be applied. Note, however, that Ingersoll & Dobrovolskis (1978) and Dobrovolskis & Ingersoll (1980) utilize the constant lag angle approach. We find both qualitative and quantitative differences with their work.

3.5. Linear Perturbation Theory

For large forcing frequencies, the time-dependent temperature and flux changes are small compared to the time-average values. One may then treat the time-dependent changes $\delta T(y, \theta, \phi, t)$ and $\delta F(y, \theta, \phi, t)$ as linear perturbations about the time-independent background values $T(y, \theta)$ and $F(y, \theta)$.

The background model is computed by integrating

$$\frac{dT}{dy} = \frac{\kappa F}{16\sigma_{\text{sb}} T^3 \Lambda} \quad (29)$$

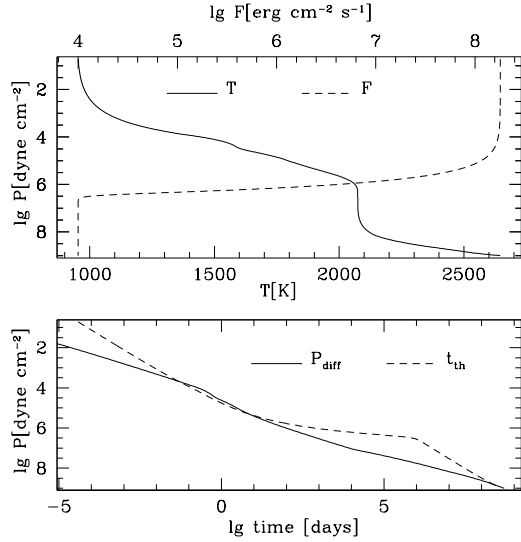


FIG. 6.— Background model constructed using time-averaged heating rate, using $\kappa_* = 10^{-2.5} \text{cm}^2 \text{g}^{-1}$, $F_{\text{core}} = 10^4 \text{erg cm}^{-2} \text{s}^{-1}$, $g = 10^3 \text{cm s}^{-2}$, a solar-type star and $P_{\text{orb}} = 4$ days.

with flux found by integrating eq.18

$$F(y, \theta) = F_{\text{core}} + \int_y^\infty dy' \epsilon(y', \theta)$$

$$= F_{\text{core}} + \frac{F_*(a) \sin \theta X_0^{10}(e)}{\pi} \int_0^{\pi/2} d\phi \cos \phi e^{-(\kappa_* y / \sin \theta) \sec(3\theta)}$$

and subject to the boundary condition $T \simeq (F(0, \theta)/4\sigma_{\text{sb}})^{1/4}$ at small optical depth. We construct this model by integrating inward from the surface. An example is given in figure 6. Our treatment of radiative transfer is simplified, but nevertheless reproduces the main features of full solutions to the transfer equations. At small optical depth the solution becomes isothermal at the “skin” temperature. Heating by inward-going stellar photons, here through the heating function, generates an equal outward flux of thermal photons (for the time-independent case). At a column $y \simeq \kappa_*^{-1}$, the heating function and outward flux decrease exponentially, and the temperature profile becomes isothermal at $T(\kappa_*^{-1}, \theta) \simeq (F(0, \theta)/\sigma_{\text{sb}})^{1/4} (\kappa/\kappa_*)^{1/4}$. Lastly, the flux F_{core} from deep in the atmosphere eventually causes the temperature to increase inward, the gradient becoming steep enough to cause convection.

The linearized equations are found by perturbing eq.9 and 10 while enforcing strict hydrostatic balance for the perturbations, so that each fluid element remains at constant y . We eliminate dependence on ϕ and t by expanding δT and δF in in a Fourier series (e.g., eq.17). The time dependence of the perturbations is then $d/dt = -i\sigma_{mk}$. We will suppress m and k in the following equations. The linearized form of eq.9 and 10 are

$$\frac{\partial \delta T}{\partial y} = \frac{dT/dy}{1 - \Lambda_R} \left[\frac{\delta F}{F} + \{\kappa_T - 3 - \Lambda_R(\kappa_T + 1)\} \frac{\delta T}{T} \right] \quad (31)$$

and

$$\frac{d\delta F}{dy} = -i\sigma C_p \delta T - \delta \epsilon, \quad (32)$$

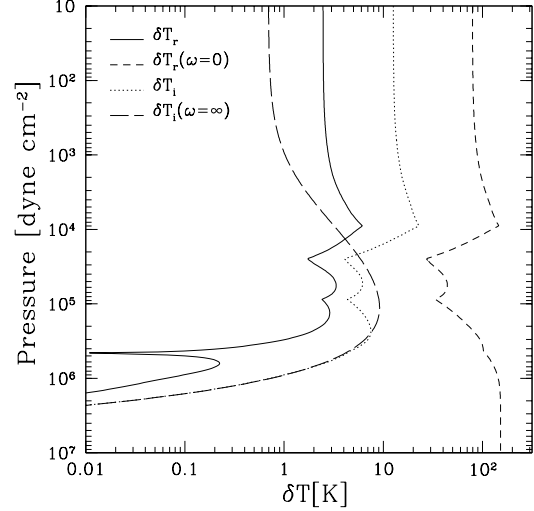


FIG. 7.— Semi-diurnal ($m = 2$), linear temperature perturbations for a planet at $P_{\text{orb}} = 4$ days with a prograde rotation rate of $P_{\text{spin}} = 1.0$ day, giving a semi-diurnal forcing period of $2/3$ day. Surface gravity is $g = 10^3 \text{cm s}^{-2}$, $\theta = \pi/2$, and $\kappa_* = 10^{-2.5} \text{cm}^2 \text{g}^{-1}$. The high frequency limit from eq.38 is a good approximation for $P \gtrsim 10^4 \text{dyne cm}^{-2}$.

where $\kappa_T = \partial \ln \kappa / \partial \ln T|_P$ and

$$\Lambda_R = \frac{R^2(R+4)}{(6+3R+R^2)(2+R)}. \quad (33)$$

At large (small) optical depth, $\Lambda_R \rightarrow 0$ (1). We solve eq.31 and 32 subject to the boundary conditions $\delta F/F = 4\delta T/T$ at the top of the grid and $\delta T, \delta F \rightarrow 0$ at the base. The equations are solved by finite difference in y to obtain a banded matrix equation which is readily inverted to find the response δT and δF to the heating $\delta \epsilon$. The top of the grid is set at a column 10^{-2} times smaller than the thermal photosphere, and the base of the grid is set at the radiative-convective boundary, typically well below $y = \kappa_*^{-1}$.

Given the temperature perturbation, the density perturbation is $\delta \rho / \rho = -\delta T / T$ at constant pressure. To linear order, the effective column is given by

$$\Sigma(\theta) = \int_0^\infty dy \left(-\frac{\delta T(y, \theta)}{T(y, \theta)} \right), \quad (34)$$

implying that the temperature perturbations *lagging* the heating tend to torque the planet away from synchronous rotation.

Examples of the solution of the linearized equations are shown in figures 7 and 8, along with analytic approximations to be discussed presently. The difference between these two plots is mainly due to the depth of heating, i.e. deep in figure 7 and shallow in figure 8.

For the deep heating case in figure 7, the forcing period ($= 2/3$ day) was chosen to be shorter than the diffusion time for the base of the heated layer. There is no time for diffusion to transport heat, the $\partial F / \partial y$ term in eq.9 is small, and the temperature fluctuates solely due to the time-dependent heating. A longer forcing period leads to larger input of heat, and effective column $\Sigma \propto P_f$, where $P_f = 2\pi/|\sigma|$ is the forcing period. An analytic solution will be presented in §3.6. Since the imaginary

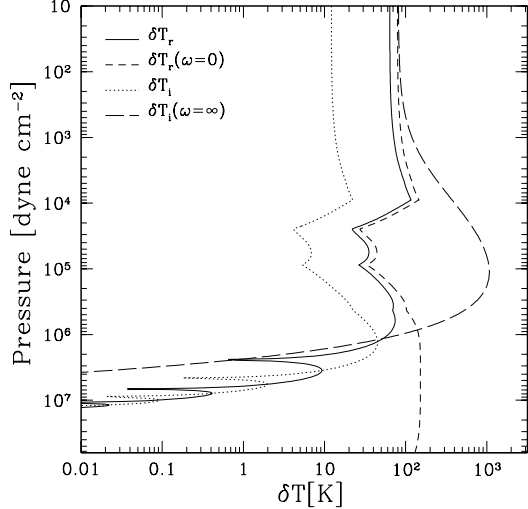


FIG. 8.— Same as figure 7 but with a spin period $P_{\text{spin}} = 3$ days and shallow heat deposition $\kappa_* = 10^{-0.5} \text{ cm}^2 \text{ g}^{-1}$. The low frequency limit is a good approximation for $P \leq 10^6 \text{ dyne cm}^{-2}$, below which the oscillations in the real and imaginary part are evidence of a diffusion wave.

part of the temperature perturbation is large only above $P_{\text{base}} = g/\kappa_*$, the torques will extend down to P_{base} .

The shallow case in figure 8, on the other hand, has a sufficiently long forcing period (6 days) that the perturbations extend deeper than P_{base} by some 2 orders of magnitude in pressure. For pressures $P \lesssim 10^6 \text{ dyne cm}^{-2}$, the first term in eq.9 can be ignored due to the small forcing frequency. In this limit, the atmosphere responds in phase to the forcing, changing quasi-statically from one equilibrium to another. No torque is exerted on the atmosphere in this limit since the temperature perturbation is in phase with the heating function. That is, for the semi-diurnal mode, temperature maxima occur at noon and midnight, while temperature minima take place at sunrise and sunset. In this “ $\sigma = 0$ ” limit, we can solve for the (real) temperature perturbation by integrating eq.9 with $dT/dt = 0$. In this regime, the thermal inertia of the material is small in comparison to the amount of photon energy absorbed per cycle and therefore, the temperature is “locked” to the heating function. For the forcing frequencies of interest, this limit will always be invalid sufficiently deep in the envelope, at which point the solution is well described by a diffusion wave. This wave is apparent in figure 8 in the region $P = 10^6 - 10^7 \text{ dyne cm}^{-2}$, where the real and imaginary parts are comparable, and exhibit oscillations. The first and second terms in eq. 9 are comparable for diffusion waves below the base of the heating layer. The decay of the envelope of this wave into the planet determines the column to which torque is applied.

Using dimensional analysis on eq.9 and 10, heat can diffuse down to a column

$$y_{\text{diff}} = \sqrt{\frac{16\sigma_{\text{sb}}T^3}{3\kappa C_p|\sigma|}} \quad (35)$$

in a forcing period $P_f = 2\pi/|\sigma|$. This depth is to be compared to the base of the heating layer at κ_*^{-1} . Heating

can diffuse below the base of the heating layer when

$$\begin{aligned} P_f &\gtrsim P_{\text{diff}} = \frac{3\pi}{8} \frac{\kappa C_p}{\sigma_{\text{sb}}T^3\kappa_*^2} \\ &= 3.6 \text{ days} \left(\frac{\kappa}{0.1 \text{ cm}^2 \text{ g}^{-1}} \right) \\ &\times \left(\frac{0.01 \text{ cm}^2 \text{ g}^{-1}}{\kappa_*} \right)^2 \left(\frac{2000 \text{ K}}{T} \right)^3. \end{aligned} \quad (36)$$

In the low frequency limit, the effective column

$$\Sigma \sim y_{\text{diff}} \propto P_f^{1/2}, \quad (37)$$

which increases more slowly as $P_f \rightarrow 0$ than the high frequency limit.

Close to the star, where the gravitational tide is large, the equilibrium spin must be in the long forcing period limit, and far from the star, where the gravitational torque is small, the equilibrium spin must be in the short forcing period limit. The dividing line between these two limits depends on factors such as stellar flux, opacities and tidal Q .

Unless $\partial T/\partial y = T/y$, the “diffusion depth”, y_{diff} , differs from the often-used “cooling depth”, $y_{\text{cool}} = F/(C_p T|\sigma|)$. See the lower panel in figure 6 for a numerical example. In the problem at hand, y_{cool} and y_{diff} can differ by orders of magnitude, especially at small optical depths and below the base of the heating layer where the flux drops exponentially. Physically, y_{cool} is the depth down to which the heat content can be radiated in the timescale $2\pi/|\sigma|$. In the absence of heating, the flux tends to become constant with depth for $y \lesssim y_{\text{cool}}$ (e.g. Piro et al. 2005). As we will show in the next sections, y_{diff} is the depth down to which small perturbations can propagate, and hence is the more relevant for heating deep in the atmosphere.

3.6. Analytic solution in the high frequency limit:

$$\sigma t_{\text{th}} \gg 1$$

The thermal time at the base of the absorbing layer, $t_{\text{th}} \sim C_p T/\kappa_* F_*$, is the timescale over which the layer can heat or cool. For large forcing frequencies $\sigma t_{\text{th}} \gg 1$, heat cannot diffuse over significant distances in a forcing period and the term $d\delta F/dy$ can be ignored. In this limit, the temperature perturbation is determined solely by the local heating function (eq.32), i.e.,

$$\delta T_{mk} = i \frac{\delta \epsilon_{mk}}{\sigma_{mk} C_p}, \quad (38)$$

where $\delta \epsilon_{mk}$ is the appropriate Fourier coefficient in eq.17. This expression shows that the temperature perturbations are small in the high frequency limit, δT decreases exponentially below $y = \kappa_*^{-1}$ and its magnitude increases with forcing period since there is more time to absorb heat. With respect to the forcing frequency σ_{mk} , the temperature perturbation lags the forcing by 90° in phase. It is compared to the solution of the linearized boundary value problem in figure 7.

The effective column is then

$$\Sigma_{mk}(\theta) \simeq -\frac{i}{\sigma_{mk} C_p} \int_0^\infty dy \left(\frac{\delta \epsilon_{mk}(y, \theta)}{T(y, \theta)} \right). \quad (39)$$

Since $T(y, \theta)$ varies relatively slowly for $y \lesssim \kappa_*^{-1}$, we approximate it as a constant and pull it out of the integral. The remaining integral is

$$\int_0^\infty ds g_m(s) \equiv G_m, \quad (40)$$

where $G_0 = 1/\pi$ and $G_2 = 1/3\pi$. Plugging eq.40 into eq.39 we find

$$\Sigma_{mk}(\theta) \simeq -i \frac{F_*(a) X_k^{1m}(e) G_m \sin \theta}{\sigma_{mk} C_p T}. \quad (41)$$

For the diurnal (semi-diurnal) component, eq.41 implies Σ leads the heating function by $\pi/2$ ($\pi/4$) in longitude. This phase lead corresponds to 6am (9am) for the maxima of the diurnal (semi-diurnal) components in figure 5.

The quadrupole moments require the angular integrals

$$F_{\ell m} = 2\pi \int_0^\pi d\theta \sin^2 \theta Y_{\ell m}(\theta, 0). \quad (42)$$

For example, $F_{22} = \sqrt{15\pi/2}(3\pi/16)$ and $F_{20} = (-\pi/16)\sqrt{5\pi}$. The final result for the quadrupole moments in the high frequency limit is

$$\text{Im} \left(\mathcal{Q}_{\ell m k}^{(\text{TT})} \right) = - \frac{R_p^{2+\ell} F_*(a)}{\sigma_{km} C_p T} X_k^{1m}(e) F_{\ell m} G_m, \quad (43)$$

confirming the order of magnitude estimates found in eq.3 and 4 if we set $\Delta M = R_p^2/\kappa_*$, $t_{\text{th}} = C_p T/\kappa_* F_*(a)$ and $\delta = 1$.

Eq.43 agrees with the quadrupole moment found in Ingersoll & Dobrovolskis (1978), up to the uncertainty as to what value of temperature should be used when it is pulled out of the integral. These authors derived the high frequency limit appropriate for a circular orbit and asynchronous rotation, and implicitly assumed a finite atmosphere bounded below by a hard surface. Eq.43 generalizes their result to a deep atmosphere, and allows for an eccentric orbit.

3.7. Analytic solution in the low frequency limit:

$$\sigma t_{\text{th}} \ll 1$$

We now consider the low frequency limit $\sigma t_{\text{th}} \ll 1$, in which the thermal time in the layer directly heated by insolation ($y \lesssim \kappa_*^{-1}$) is short compared to the forcing period. The small thermal inertia of the absorbing layer implies that temperature perturbations are large and in phase with the forcing, with corresponding density perturbations 180° out of phase with the insolation, implying that the torque is zero. There will always be a layer at $y \gtrsim \kappa_*^{-1}$ sufficiently deep that the thermal time becomes longer than the forcing period, and the temperature perturbation in this deep layer will be out of phase, yielding a torque.

To illustrate this, we divide the atmosphere into two separate plane-parallel layers, as depicted in Figure 9. The stellar flux is absorbed in the upper layer at a column $y \sim \kappa_*^{-1}$, and generates an outward flux of thermal radiation. In the lower layer, the stellar flux is negligible, and time-dependent temperature perturbations can only penetrate this layer due to thermal diffusion.

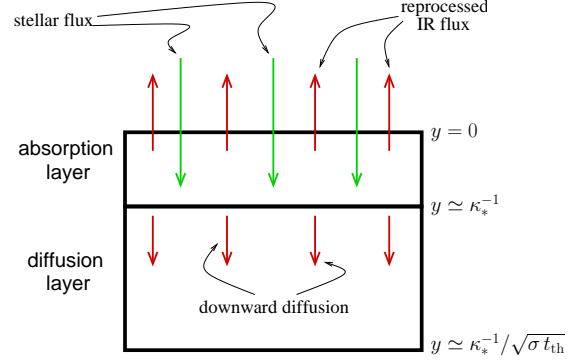


FIG. 9.— Cartoon depicting time-dependent heating in the limit where the forcing period, $2\pi/\sigma$, is large in comparison to the thermal time t_{th} of the absorption layer. The temperature of the absorption layer is approximately “locked” to the time-varying insolation such that the maxima in temperature take place at noon for diurnal heating and noon and midnight for semi-diurnal heating. However, a thermal diffusion wave penetrates to a column depth $y \sim y_{\text{diff}} = \kappa_*^{-1}/\sqrt{\sigma t_{\text{th}}}$. As expected for a thermal diffusion wave, the temperature fluctuation at $y \sim y_{\text{diff}}$ lags the temperature fluctuation in the absorption layer by $\pi/4$ in phase, which ultimately allows the heated layers to couple to the semi-diurnal tidal field in such a way as to increase its spin angular momentum.

The thermal time in the upper layer is short, and the time derivative term in eq. 32 can be set to zero. The temperature profile changes quasi-statically in response to changes in the heating rate. As an analytic example, consider a flux profile $F(y) = F_0 \exp(-\kappa_* y)$ and constant opacities κ and $\kappa_* \ll \kappa$. The temperature deep in the layer is then $T \simeq (3\kappa F_0/4\sigma_{\text{sb}}\kappa_*)^{1/4}$. If the heating produces a change in flux $F_0 \rightarrow F_0 + \delta F_0$, the fractional change in temperature deep in the upper layer is

$$\frac{\delta T}{T}(y = \kappa_*^{-1}) \simeq \frac{\delta F_0}{4F_0}. \quad (44)$$

For semi-diurnal forcing, the fact that δT reaches its maximum at noon and midnight implies that $\delta\rho$, or the thermal tidal bulge, achieves its maximum value at sunrise and sunset. As result, the gravitational tidal field cannot apply a torque to the the thermal tidal bulge induced in the upper layer in the $\sigma t_{\text{th}} \ll 1$ limit.

Direct heating is negligible in the lower layer, and $\delta\epsilon$ in eq. 32 may be set to zero. Therefore, the temperature perturbation is determined by a source-free diffusion equation subject to the boundary condition in eq.44 at $y = \kappa_*^{-1}$. The background temperature T is roughly constant below $y = \kappa_*^{-1}$, and we assume constant opacity κ for simplicity. With this, the temperature perturbation in the lower diffusion layer obeys

$$-i\sigma C_p \delta T = \frac{16\sigma_{\text{sb}}^3 T^3}{3\kappa} \frac{d^2 \delta T}{dy^2} \quad (45)$$

over the interval $\kappa_*^{-1} \leq y \leq \infty$. The general solution of eq.45 has the form

$$\frac{\delta T}{T} = C e^{s(y-\kappa_*^{-1})} + D e^{-s(y-\kappa_*^{-1})} \quad (46)$$

where

$$s = e^{-i\pi/4} \sqrt{\frac{3\kappa\sigma C_p}{16\sigma_{\text{sb}} T^3}} \quad (47)$$

is the wavenumber, in units of inverse column. Note that

σ may be either positive or negative in this expression. Finiteness of the solution at $y = \infty$ implies $C = 0$ for either sign of σ . The final result for the temperature perturbation in the lower layer is then

$$\frac{\delta T}{T}(y) = \frac{\delta F_0}{4F_0} e^{-s(y-\kappa_*^{-1})}. \quad (48)$$

Since s is complex, eq.48 implies oscillations in temperature, as well as an envelope decreasing to larger depths. These oscillations are apparent in the linear solution in figure 8, as well as in the nonlinear solution in figure 2.

The effective column is determined by integrating eq.48 over the lower layer to find

$$\begin{aligned} \Sigma &= - \int_{\kappa_*^{-1}}^{\infty} dy \frac{\delta T}{T} \simeq - \left(\frac{\delta F_0}{4F_0} \right) \left(\frac{1}{s} \right) \\ &= -e^{i\pi/4} \left(\frac{\delta F_0}{4F_0} \right) \sqrt{\frac{16\sigma_{\text{sb}} T^3}{3\kappa\sigma C_p}} \end{aligned} \quad (49)$$

which leads in phase by $3\pi/4$, as compared to $\pi/2$ for the high frequency limit. For the diurnal (semi-diurnal) component, eq.49 implies Σ leads the heating function by $3\pi/4$ ($3\pi/8$) in longitude. This phase lead corresponds to 3am (7:30am) for the maxima of the diurnal (semi-diurnal) components in figure 5.

Combining the results from §3.6 and this section, we find generically that the semi-diurnal component of Σ , and hence the quadrupole moments, have the *opposite* phase as the gravitational tide quadrupole moments. Hence they promote asynchronous spin, and may drive eccentricity. Furthermore, eq.49 shows that Σ continues to increase as the forcing frequency goes to zero, albeit with a shallower power of σ . We summarize the scalings from eq.41 and 49 by writing

$$\Sigma \sim \kappa_*^{-1} \text{Min}[(\sigma t_{\text{th}})^{-1}, (\sigma t_{\text{th}})^{-1/2}], \quad (50)$$

and phase lead in the range $\pi/2 - 3\pi/4$.

4. EQUILIBRIUM SPIN RATE

Hot Jupiters are commonly assumed to be very nearly synchronized. The argument is that the synchronization timescale, for $Q'_p = 10^6$, is far shorter than the age of observed planets. The torque on the planet due to the gravitational tide is given by (eq.28 and A18)

$$\begin{aligned} N^{(\text{GT})} &= \left(\frac{9}{2} \right) \left(\frac{n}{Q'_p} \right) \left(\frac{M_*^2}{M_* + M_p} \right) \left(\frac{R_p^5}{a^3} \right) (n - \Omega) \\ &= -7 \times 10^{32} \text{ erg } R_{10}^5 \left(\frac{10^6}{Q'_p} \right) \left(\frac{P_{\text{orb}}}{4 \text{ days}} \right)^{-4} \left(\frac{\Omega - n}{n} \right) \end{aligned} \quad (51)$$

for a circular orbit. Starting from a rapid initial spin rate $\Omega_0 \gg n$, the synchronization time is

$$\begin{aligned} t_{\text{synch,GT}} &= - \frac{I_p \Omega_0}{N^{(\text{GT})}} = \frac{2}{9} \eta \left(\frac{Q'_p}{n} \right) \left(\frac{M_p (M_* + M_p)}{M_*^2} \right) \left(\frac{a^3}{R_p^3} \right) \\ &= 10^5 \text{ yr} \left(\frac{\eta}{0.25} \right) \left(\frac{Q'_p}{10^6} \right) \left(\frac{2.8 \text{ hr}}{P_p} \right)^2 \left(\frac{P_{\text{orb}}}{4 \text{ days}} \right)^3 \end{aligned} \quad (52)$$

where $I_p = \eta M_p R_p^2$, $\eta \simeq 0.25$ is appropriate for Jupiter-like planets, and we have defined the ‘‘dynamical time’’

$P_p = 2\pi(R_p^3/GM_p)^{1/2}$. Hence, for $Q'_p = 10^6$, planets out to $P_{\text{orb}} \sim 150$ days should be synchronized in 5 Gyr.

The fact that gas giants have $Q'_p \sim 10^6$ implies gravitational tides are far *weaker* than for terrestrial type planets with $Q'_p \sim 10 - 100$. Additional torques are relatively more important for gas giants in comparison to terrestrial planets. We now show that thermal tidal torques are capable of generating significant asynchronous spin for hot Jupiters.

The high frequency limit has a simple analytic solution. For zero eccentricity, plugging the $\ell = m = k = 2$ quadrupole moments from eq.43 into eq.A23 gives the thermal tide torque in the high frequency limit

$$N^{(\text{TT})} = \frac{3\pi}{16} \frac{n^2 R_p^4 F_*}{(\Omega - n) C_p T}. \quad (53)$$

Recall that T should be evaluated at $y \sim \kappa_*^{-1}$, and here $F_* = F_*(a)$. This estimate agrees with that of Ingersoll & Dobrovolskis (1978). Plugging in numbers for a solar-type star we find

$$N^{(\text{TT})} = 2.8 \times 10^{32} \text{ erg} \left(\frac{n}{\Omega - n} \right) \left(\frac{4 \text{ days}}{P_{\text{orb}}} \right)^2 R_{10}^4 f_T^3 \quad (54)$$

where $R_{10} = R/10^{10}$ cm and $f_T = T/(F_*/\sigma_{\text{sb}})^{1/4}$. Clearly for the hot Jupiters the gravitational tide torque in eq.51 and the thermal tide torque in eq.54 are comparable. Equating eq.54 and 51 we find the equilibrium spin rate

$$\Omega_{\text{eq}} = n \left(1 \mp \sqrt{\frac{\pi}{24} \frac{F_*}{C_p T} \frac{G Q'_p}{n^3 R_p}} \right) \quad (55)$$

or, numerically

$$P_{\text{spin,eq}} = \frac{P_{\text{orb}}}{\left(1 \pm 0.63 \left(\frac{P_{\text{orb}}}{4 \text{ days}} \right) \left(\frac{Q'_p}{10^6} R_{10}^{-1} f_T^{-1} \right)^{1/2} \right)} \quad (56)$$

The \mp sign denotes the subsynchronous ($\Omega < n$) and supersynchronous ($\Omega > n$) solutions. The subsynchronous solution becomes retrograde ($\Omega < 0$) for sufficiently long P_{orb} . Eq.56 shows that the degree of asynchronous spin increases for larger P_{orb} and is large for the hot Jupiters for $Q \sim 10^5 - 10^6$. At long orbital period, the spin period asymptotes to a constant

$$P_{\text{spin,eq}} \rightarrow \pm 6.34 \text{ days} \left(R_{10} \frac{Q'_p}{10^6} f_T^{-1} \right)^{1/2}. \quad (57)$$

If no new physics intervenes, this asymptotic spin rate should hold for planets at $P_{\text{orb}} \lesssim 150$ days which have sufficient time to attain spin equilibrium. Since the degree of asynchronous spin decreases toward the star, the high frequency limit becomes less accurate there.

Small perturbations about the equilibrium spin rate, at fixed P_{orb} and R_p , are stable for both the super- and sub-synchronous solutions given above.

The accuracy of the high frequency limit can be estimated analytically. The semi-diurnal ($m = 2$) forcing period in the high frequency limit is

$$P_f = 3.2 \text{ days } R_{10}^{1/2} \left(\frac{10^6}{Q'_p} \right)^{1/2}, \quad (58)$$

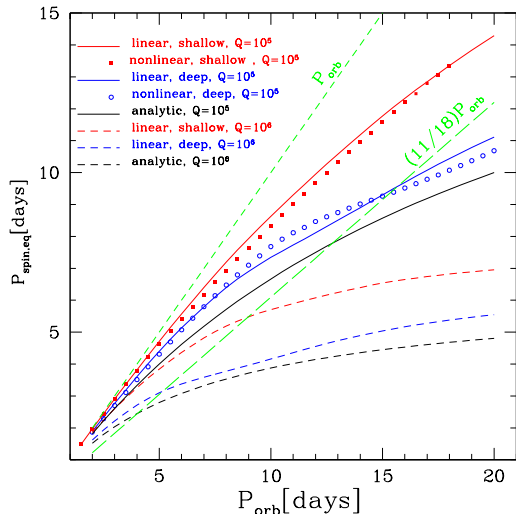


FIG. 10.— Equilibrium spin period as a function of orbital period for super-synchronous solutions ($\Omega > n$). The “shallow” and “deep” lines represent $\kappa_* = 10^{-0.5}, 10^{-2.5} \text{ cm}^2 \text{ g}^{-1}$, respectively. The solid black line is the analytic model from §3.6 with $f_T = 1$. The short-dashed green line is the orbital period, and the long-dashed green line shows $P_{\text{spin}} = (11/18)P_{\text{orb}}$, the spin period below which the gravitational tide excites eccentricity. Surface gravity is $g = 10^3 \text{ cm s}^{-2}$ and radius is $R_p = 10^{10} \text{ cm}$. The flux from the core is taken to be $F_{\text{core}} = 10^4 \text{ erg cm}^{-2} \text{ s}^{-1}$, independent of latitude.

independent of orbital period. The diffusion time to the base of the heating layer is (eq.36)

$$P_{\text{diff}} \simeq 1.6 \text{ days} \left(\frac{P_{\text{orb}}}{4 \text{ days}} \right) \left(\frac{10^{-2.5} \text{ cm}^2 \text{ g}^{-1}}{\kappa_*} \right). \quad (59)$$

At long orbital periods, the forcing period becomes shorter than the diffusion time, and the high frequency limit is applicable. Equating the expressions in eq.58 and 59 a rough estimate for the applicability of the high frequency limit is

$$P_{\text{orb}} \geq 8 \text{ days} R_{10}^{1/2} \left(\frac{10^6}{Q'_p} \right)^{1/2} \left(\frac{\kappa_*}{10^{-2.5} \text{ cm}^2 \text{ g}^{-1}} \right) \quad (60)$$

The high frequency limit allows useful analytic intuition, but neglects diffusion and approximates temperature at the base as constant. We now present results on equilibrium spin rate and heating rate relaxing these assumptions. Note, however, that these calculations are not fully self-consistent in that we fix a radius, and we also take, for simplicity, the flux from the core to be constant, independent of latitude. In §7 we will self-consistently determine the radius in thermal equilibrium and determine the self-consistent value of F_{core} .

Figure 10 shows equilibrium spin rate for three different methods of calculation: “nonlinear simulations” as discussed in §3.1 and 3.3, “linear” calculations solving the linearized equations as a boundary value problem (§3.5), and the “analytic” result from eq.56 in the high frequency limit. Two different heating depths are shown, “shallow” and “deep” lines, as well as two different values for the tidal Q . The good agreement between linear and nonlinear calculations implies that at the large depths where the quadrupole moments are determined, nonlinear effects do not greatly change the result. The analytic

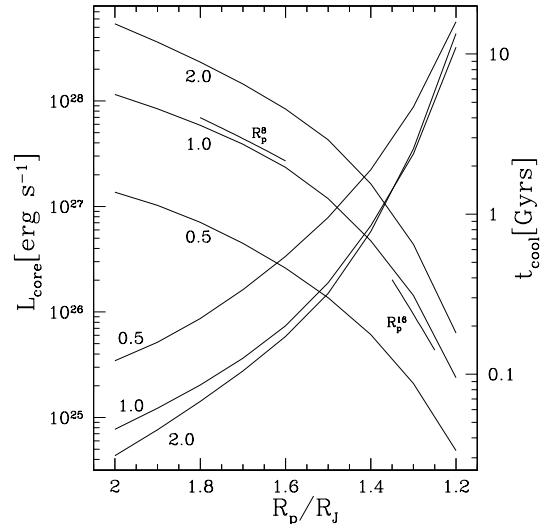


FIG. 11.— Cooling luminosity from the core (curves sloping up to the left) and cooling time (curves sloping up to the right) versus planetary radius for three different planetary masses, $M_p/M_J = 0.5, 1.0, 2.0$. A solar type star is used and the planets sit at $P_{\text{orb}} = 2$ days. The heating depth is given by $\kappa_* = 10^{-2} \text{ cm}^2 \text{ g}^{-1}$. Closer to the star, insolation is larger and L_{core} decreases, and visa versa further from the star.

approximation is accurate to within $\sim 10\%$. The degree of asynchronous spin is large for both $Q'_p = 10^5$ and 10^6 cases. The shallow heating case is more nearly synchronized than the deep heating case as it is more in the low frequency limit than the deep heating case, and hence the thermal tide torque is weaker.

5. TIDAL HEATING RATES

The large tidal heating rates for eccentric hot Jupiters can inflate the radii of these planets if heat is deposited in the convective core, or slow their cooling if heat is deposited in the radiative envelope (Bodenheimer et al. 2001). Previous investigations considered transient tidal heating due to an energy reservoir in the initial eccentricity, or steady-state heating due to eccentricity pumped by a companion. In this section we compute gravitational tidal heating rates due to the asynchronous spin set by a balance of gravitational and thermal tide torques for a planet on a circular orbit. We compare these heating rates to the cooling rate of the core to determine if tidal heating can power the large observed radii.

Appendix B describes an updated version of the planetary structure and evolution models of Arras & Bildsten (2006). Figure 11 shows the cooling luminosity of the convective core as a function of radius for $P_{\text{orb}} = 2$ days around a Sun-like star. Also shown is the timescale to attain thermal equilibrium

$$t_{\text{cool}} = \frac{\int_0^{M_p} dm C_p T}{L_{\text{core}}}. \quad (61)$$

Cooling timescales for Jupiter-mass planets become shorter than a typical age of 3 Gyr for $R_p \gtrsim (1.3 - 1.4) \times R_J$. Cooling rates closer (further) from the star are lower (higher) due to the insulation effect.

Models for the passive cooling of irradiated hot Jupiters can typically explain planets with radii $R \lesssim 1.2R_J$ and below, but have difficulty slowing the cool-

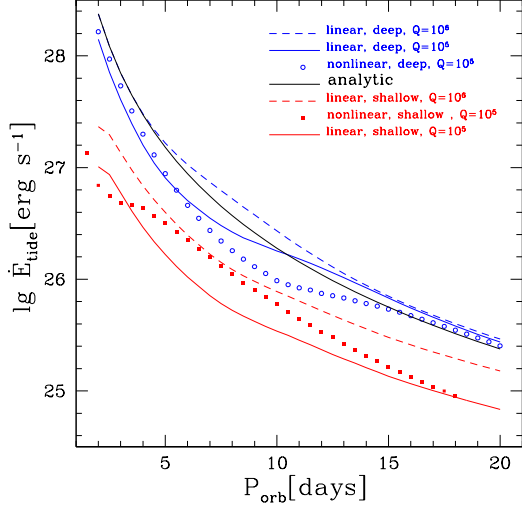


FIG. 12.— Gravitational tide heating rate for the equilibrium spin periods shown in figure 10.

ing enough to explain planets with $R \gtrsim 1.2R_J$ (e.g. Fortney 2008). If we are interested in the radius range $R = (1.2 - 1.8) \times R_J$, figure 11 shows this corresponds to core cooling rates of $10^{25} - 10^{28} \text{ erg s}^{-1}$, depending on mass and insolation level. In order for tides to halt the cooling of the core, this loss of heat at the radiative-convective boundary must be balanced by a gain of heat in the core due to tides.

The tidal heating rate in eq.A21 is related to the torque in eq.A18 by the pattern speed $(kn - m\Omega)/m$ for each harmonic. In spin equilibrium, with $N^{(\text{TT})} = -N^{(\text{GT})}$, the gravitational tide heating rate for the high frequency limit is

$$\begin{aligned} \dot{E}_{\text{heat}}^{(\text{GT})} &= (n - \Omega)N^{(\text{GT})} \\ &= 2.9 \times 10^{27} \text{ erg s}^{-1} \left(\frac{4 \text{ days}}{P_{\text{orb}}} \right)^3 R_{10}^4. \end{aligned} \quad (62)$$

The tidal heating rate in the high frequency limit is independent of Q since $\Omega - n \propto (Q'_p)^{1/2}$ and $\dot{E} \propto (\Omega - n)^2/Q'_p$.

Figure 12 shows the tidal heating rates for the equilibrium spin rates in figure 10. The same small deviations between the linear and nonlinear results are apparent in this figure, but note that for the deep heating case the nonlinear, linear and analytic (high frequency limit) results agree at large orbital period. The shallow heating case shows a smaller heating rate than the deep heating case as the torque is smaller. Recall that the tidal heating rate is independent of Q'_p in the high frequency limit. This agrees with the deep heating case for large P_{orb} . Somewhat counterintuitively, *larger* Q'_p leads to a larger tidal heating rate at smaller P_{orb} when thermal diffusion effects become important. The dependence of spin and heating rates on Q'_p can be understood simply. Let $N^{(\text{TT})} = a(n)(\Omega - n)^{-\alpha}$ and $N^{(\text{GT})} = -b(n)(\Omega - n)^\beta Q^{-1}$, for some functions a and b of orbital period, and exponents α and β . The equilibrium spin rate is

$$\Omega_{\text{eq}} - n = \left(\frac{aQ}{b} \right)^{1/(\alpha+\beta)} \quad (63)$$

and the tidal heating rate is

$$\dot{E}_G = (\Omega - n)^{1+\beta} b Q^{-1} = a^{(\beta+1)/(\beta+\alpha)} (Q/b)^{(1-\alpha)/(\beta+\alpha)} \quad (64)$$

In the high frequency limit, for Darwin's theory of tides, $\alpha \simeq 1$ and $\beta \simeq 1$ give $\Omega_{\text{eq}} - n \propto Q^{1/2}$ and $\dot{E} \propto Q^0$. In the low frequency limit, diffusion leads to $\alpha \sim 1/2$ so that $\Omega_{\text{eq}} - n \propto Q^{2/3}$ and $\dot{E} \propto Q^{1/3}$, i.e. heating rate increases with Q . Lastly note that even varying Q by an order of magnitude and the heating depth by two orders of magnitude the dissipation rate varies by less than one order of magnitude, and is in the range $\dot{E} \simeq 10^{26} - 10^{28} \text{ erg s}^{-1}$ for hot Jupiters at $P_{\text{orb}} \lesssim 5$ days. This heating rate is sufficient to explain the large radii of hot Jupiters, as seen by comparing figures 11 and 12.

Thermal equilibria are stable to small perturbations in R_p if the perturbation to cooling dominates that of heating. If $\dot{E}_{\text{heat}}^{(\text{GT})} \propto R_p^c$ and $L_{\text{core}} \propto R_p^d$, thermal stability requires $d > c$. The tidal heating rate in eq.62 has $c = 4$. Figure 11 shows that the cooling rate has $d \simeq 8 - 16$ over the range of radii shown, implying stability. We find, however, that at a larger radius $R_p \gtrsim 3R_J$, the exponent d becomes less than 4, implying thermal instability.

6. ECCENTRICITY EVOLUTION

The orbits of some hot Jupiters are clearly more circular than for the population of long period planets. This is often attributed to circularization by the gravitational tide raised in the planet by the star. The rate of change of eccentricity is (Mardling & Lin 2002)

$$\dot{e}^{(\text{GT})} = -e \left(\frac{81n}{2Q'_p} \right) \left(\frac{M_\star}{M_p} \right) \left(\frac{R_p}{a} \right)^5 \left(f_1(e) - \frac{11}{18} f_2(e) \frac{\Omega}{n} \right) \quad (65)$$

where

$$f_1(e) = \frac{1 + (15/4)e^2 + (15/8)e^4 + (5/64)e^6}{(1 - e^2)^{13/2}} \quad (66)$$

and

$$f_2(e) = \frac{1 + (3/2)e^2 + (1/8)e^4}{(1 - e^2)^5}. \quad (67)$$

For the equilibrium spin rate implied by $N^{(\text{GT})} = 0$ (see Hut (1981), eq.11), the bracketed factor in eq.65 is positive, implying circularization. The circularization time is then

$$\begin{aligned} t_{\text{circ,GT}} &= -\frac{e}{\dot{e}^{(\text{GT})}} = 2 \times 10^8 \text{ yrs} \left(\frac{P_{\text{orb}}}{4 \text{ days}} \right)^{13/3} \left(\frac{Q'_p}{10^6} \right) \\ &\times \left(\frac{P_p}{4 \text{ hrs}} \right)^{-10/3} \left(\frac{M_\star}{10^3 M_p} \right)^{2/3} \left(f_1(e) - \frac{11}{18} f_2(e) \frac{\Omega}{n} \right)^{-1} \end{aligned} \quad (68)$$

For hot Jupiters with radii $R = (1.0 - 1.8) \times R_J$, $Q'_p \leq 10^6$ and $P_{\text{orb}} \lesssim 5$ days the orbits should be highly circular after 5 Gyr. While many orbits are consistent with zero eccentricity, it has been emphasized by Matsumura et al. (2008) that nearly 1/4 of planets within 0.1AU have $e \geq 0.1$. In the absence of additional perturbations to the orbit, the finite eccentricity can only be explained by rather large $Q'_p \sim 10^8$. The question is then why planets with presumably similar structure and orbital periods should have tidal Q differing by orders of magnitude.

Inclusion of both the thermal and gravitational tides changes this simple picture in two ways.

First, eq.65 shows that there is a critical spin rate $\Omega = n(18/11)(f_1/f_2)$ above which the gravitational tide *excites*, rather than damps, eccentricity. For evolution only under the gravitational tide, such rapid spin rates occur only for young, rapidly rotating planets. Synchronization occurs on a timescale shorter than the circularization time by $\sim 10^3$, so that negligible eccentricity is excited in the early spin down phase. However, taking into account *both* gravitational and thermal tide torques, §4 shows that significant deviations from synchronous rotation occur in the steady state, over the entire life of the system. For $e = 0$ spin equilibrium, figure 10 shows the critical spin frequency $\Omega = (18/11)n$. For $Q'_p = 10^6$, we find the gravitational tide can drive eccentricity for $P_{\text{orb}} \gtrsim (5-9)$ days, depending on the depth of the heating layer. For $Q'_p = 10^5$ the critical orbital period is longer by a factor of a few.

Second, the thermal tide may excite eccentricity due to the fact that density *leads* the forcing. The small eccentricity ($e \ll 1$), high frequency ($\sigma t_{\text{th}} \gg 1$) limit is analytically tractable. To leading order in e , the results of §3.6 plugged into eq.A24 yield

$$\begin{aligned} \dot{e}^{(\text{TT})} = e \frac{3\pi}{16} \left(\frac{R_p^4 F_\star(a)}{M_p C_p T a^2} \right) \\ \times \left(1 + \frac{21n/2}{3n - 2\Omega} + \frac{n/2}{2\Omega - n} + \frac{n/2}{\Omega - n} \right). \quad (69) \end{aligned}$$

The four terms in the last parenthesis are the $\mathcal{O}(e)$ harmonics $(m, k) = (0, 1), (2, 3), (2, 1)$ and $(2, 2)$. Depending on Ω/n , eccentricity can either be excited or damped. Large response occur near the three resonances $P_{\text{spin}}/P_{\text{orb}} = 2/3, 1, 2$.

At small eccentricity, both the gravitational and thermal tides have $\dot{e} \propto e$, implying either exponential growth or decay with the rate (see eq.65, 69 and 55)

$$\begin{aligned} \gamma_e = \frac{\dot{e}^{(\text{GT})} + \dot{e}^{(\text{TT})}}{e} \\ = \left(\frac{81n}{2Q'_p} \right) \left(\frac{M_\star}{M_p} \right) \left(\frac{R_p}{a} \right)^5 \left[- \left(1 - \frac{11\Omega}{18n} \right) \right. \\ \left. + \frac{1}{9} \left(\frac{\Omega_{\text{eq}} - n}{n} \right)^2 \left(1 + \frac{21n/2}{3n - 2\Omega} + \frac{n/2}{2\Omega - n} + \frac{n/2}{\Omega - n} \right) \right] \quad (70) \end{aligned}$$

Figure 13 evaluates eq.70 using $\Omega = \Omega_{\text{eq}}$ for $e = 0$ from eq.56, for the supersynchronous solution (solid line) and the subsynchronous solution (dashed line). Two different tidal $Q'_p = 10^5 - 10^6$ are shown. The value of Q'_p determines how long the orbital period must be before the spin becomes sufficiently asynchronous for γ_e to change sign. In both cases shown in figure 13, the same basic pattern is found. For the supersynchronous case, close to the star eccentricity is strongly damped, then a region of eccentricity growth ending with a resonance, then a region of eccentricity damping starting with the same resonance. The eccentricity is always driven at long orbital periods, although the growth rate is too small to affect the orbit over the system's lifetime. In the regions of large eccentricity growth, even if a planet began with small e ,

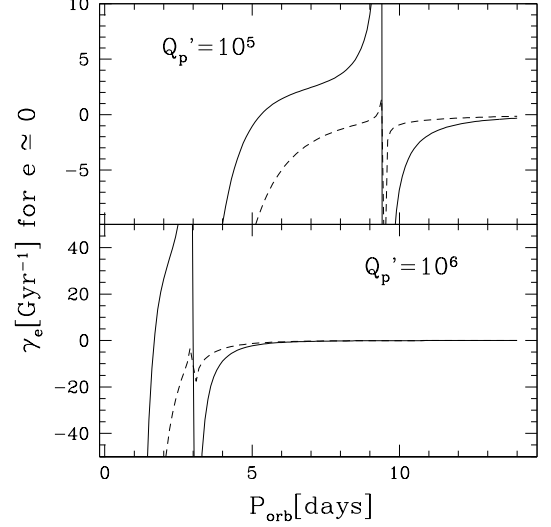


FIG. 13.— Growth rate of eccentricity e in the $e \ll 1$ limit, using the high frequency limit for the thermal tide (see eq.70) and the equilibrium spin frequencies for $e = 0$ from eq.56. Positive values denote eccentricity growth and negative values denote eccentricity damping. The solid (dashed) lines are the super-(sub-) synchronous solutions for the spin. The upper panel is for strong gravitational tide ($Q'_p = 10^5$) while the lower panel is for weak gravitational tide ($Q'_p = 10^6$). A solar type star was used, and $M_p = M_J$ and $R_p = 1.3R_J$. The divergences are due to the $(k, m) = (3, 2)$ and $(1, 2)$ resonances for the thermal tide terms in eq.70.

10-100 efoldings would imply that the eccentricity could grow to large values. For small $Q'_p = 10^5$, eccentricity may be driven even out to $P_{\text{orb}} = 10$ days, implying the observed eccentricity at these relatively large orbital periods may not be primordial, but rather influenced by the thermal tide. For the subsynchronous case, the regions of eccentricity growth are far more limited, and may be confined to orbital periods very near the resonance.

We have shown that small, but finite, eccentricity is unstable for small “windows” in P_{orb} . Hence even if all orbits began as nearly circular, a non-monotonic distribution of eccentricity would result, in which eccentricity would be small near the star, possibly large in the window where $\gamma_e > 0$, and again small in the exterior region where $\gamma_e \approx 0$. The P_{orb} range for large eccentricity may differ from one system to the next, as it depends on factors such as stellar flux and planet mass, radius and tidal Q'_p , and heating depth κ_\star^{-1} . This effect may explain the non-monotonic distribution of observed eccentricities for hot Jupiters.

7. SIMULTANEOUS SPIN, ORBIT AND THERMAL EQUILIBRIUM

In this section we self-consistently solve for the values of P_{spin} , R_p and e which satisfy

$$N^{(\text{TT})} + N^{(\text{GT})} = 0 \quad (71)$$

$$\dot{E}_{\text{heat}}^{(\text{GT})} - L_{\text{core}} = 0 \quad (72)$$

$$\dot{e}^{(\text{GT})} + \dot{e}^{(\text{TT})} = 0. \quad (73)$$

Rather than choosing fixed values of F_{core} independent of latitude, we follow appendix B to compute $F_{\text{core}}(\theta)$ by requiring that the radiative atmosphere match smoothly to an adiabatic interior with the correct M_p and R_p . Given

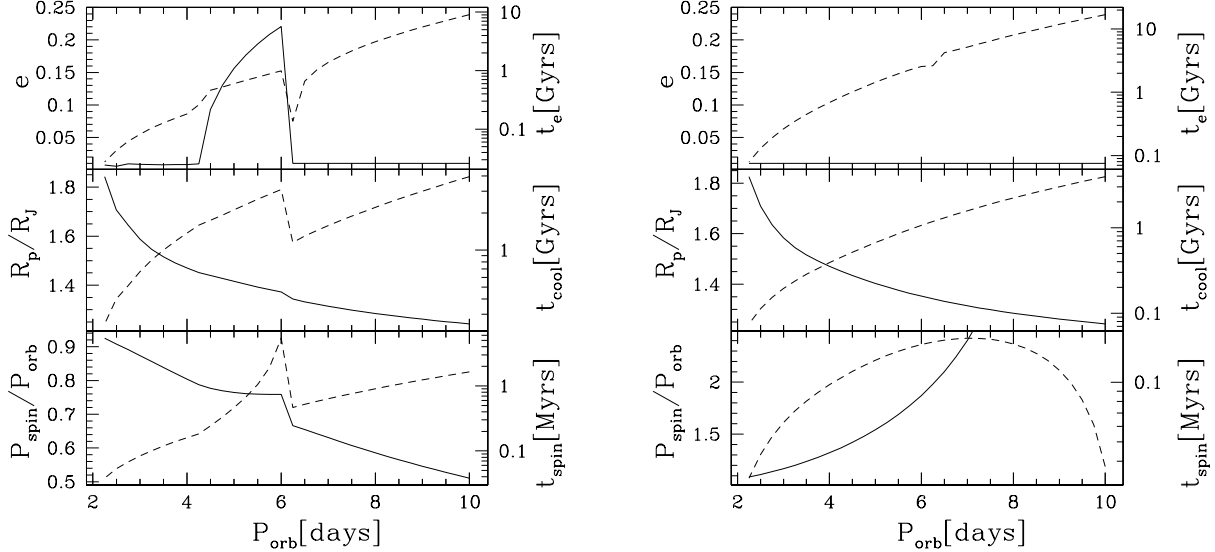


FIG. 14.— Equilibrium values of P_{spin} , R_p and e for $M_p = M_J$, $\kappa_* = 10^{-2} \text{ cm}^2 \text{ g}^{-1}$ and $Q'_p = 10^6$. The left (right) plot shows the super- (sub-) synchronous solution. In each panel, the solid line is for the left axis showing e , R_p and P_{spin} , and the dashed line is for the right axis showing the timescales to attain equilibrium.

this background solution for the atmosphere, we solve the boundary value problem for the linearized perturbations (see §3.5). This includes diffusion explicitly, and interpolates between the high and low frequency limits. The perturbations are then used to compute the quadrupole moments by integration over column (eq.34) and latitude (eq.23). Enough terms are used in the frequency sums in eq.A17, A18 and A21 to ensure convergence. Newton’s method is used find equilibrium values given a guess at the solution. We choose a small starting value for eccentricity, $e = 0.01$. If $\gamma_e > 0$, the eccentricity grows until it reaches a finite equilibrium value. If $\gamma_e < 0$ at $e = 0.01$, we treat $e = 0$ as a good equilibrium solution.

Results are shown in figure 14 for $M_p = M_J$, $\kappa_* = 10^{-2} \text{ cm}^2 \text{ g}^{-1}$ and $Q'_p = 10^6$. First we discuss the super-synchronous solution in the left panel. Close to the star, the gravitational tide dominates, resulting in nearly synchronous spin and circular orbit. The tidal heating rate due to asynchronous spin grows rapidly toward the star, leading to an increase in radius. The numerical values can be understood by comparing figures 11 and 12. In between $P_{\text{orb}} \simeq 4 - 6$ days, $\gamma_e > 0$ and $e = 0$ is not a stable equilibrium. We find finite equilibrium eccentricity with values $e = 0.0 - 0.2$. Finite eccentricity does not seem to be as important as asynchronous spin in the tidal heating rate since no feature appears between 4-6 days for R_p . The eccentricity equilibria in figure 14 are stable. For the $e = 0$ equilibria, $de/dt < 0$ implies stability. In the window of instability, $de/dt > 0$ for $e < e_{\text{eq}}$ while $de/dt < 0$ for $e > e_{\text{eq}}$.

The timescale to return to spin equilibrium for a small deviation from equilibrium is

$$t_{\text{spin}} \simeq \frac{I_p \Omega_{\text{eq}}}{N_{\text{eq}}} \quad (74)$$

where $N_{\text{eq}} = |N_{\text{eq}}^{(\text{TT})}| = |N_{\text{eq}}^{(\text{GT})}|$ is the value of the opposing torques in equilibrium. This timescale is shorter than the age by a factor $\sim 10^3$ for $P_{\text{orb}} \lesssim 1$ week. The core cooling time in eq.61 is comparable to or shorter

than the Gyr age for $P_{\text{orb}} \lesssim 10$ days. The timescale to reach eccentricity equilibrium is

$$t_e = \left(\frac{d \ln e_{\text{eq}}}{dt} \right)^{-1} \quad (75)$$

where $d \ln e_{\text{eq}}/dt = |d \ln e_{\text{eq}}^{(\text{GT})}/dt| = |d \ln e_{\text{eq}}^{(\text{TT})}/dt|$, evaluated at equilibrium. The eccentricity evolution time is also comparable to or shorter than the age inside 1 week. Close to the star, we expect all three quantities to have equilibrium values, while further away there may not be sufficient time for R_p and e to attain equilibrium values.

The sub-synchronous solution is shown in the right hand panel of figure 14. While the radius is similar to that of the super-synchronous solution, the spin and eccentricity differ. The $(m, k) = (2, 1)$ resonance is weaker than the $(m, k) = (2, 3)$ resonance due to the prefactor in eq.69, and eccentricity is driven less strongly than the super-synchronous case. At the evenly spaced orbital periods used, we did not get close enough to the resonance for the driving to be significant. The spin period becomes large for long orbital period, and will eventually turn into retrograde spin.

Although not plotted in figure 14, we found additional finite eccentricity solutions for $P_{\text{orb}} \gtrsim 6$ days, where $e = 0$ is also a solution. We have not thoroughly investigated large e equilibria which cannot be found from a small starting guess for e . We leave this for a future investigation, but note that many equilibria may be possible due to higher order thermal tide resonances that become important for large e . The ability to trap the orbit into one of these resonances during evolution will require a more detailed numerical investigation.

We now discuss how the results in figure 14 would change for different parameters. From figure 11, increasing M_p leads to larger cooling rates at fixed R_p . To bring heating ($\propto R_p^4$) and cooling ($\propto M_p R_p^{8-16}$) back into balance requires that higher mass planets must have smaller radii, and vice versa for lower mass planets. For

smaller Q'_p (larger gravitational tide dissipation rate), the planet must be further from the star before significant asynchronous spin develops. This pushes the strong resonance driving eccentricity further from the star (see figure 13), with a drop in the magnitude of the driving rate. Increasing $F_*(a)$ and e , and decreasing κ_* , acts to increase the strength of the thermal tide, pushing the spin away from synchronous and the region of $\gamma_e > 0$ closer to the star where γ_e is larger.

Our calculations are successful from the point of view that we have identified a powerful internal heat source which may explain the large radii observed for the transiting planets. However, our theory predicts a correlation of radius with orbital period, and nonzero eccentricity over a small range in orbital period. The plots of R_p and e versus P_{orb} for the observed transiting planets do not clearly show the simple behavior found in figure 14. We speculate that part of the variance is due to differences in planet mass, stellar flux and heating depth (κ_*) associated with the TiO/VO transition. Furthermore, our radii are upper limits, as we do not include a core. We intend to make more detailed comparison to data in a future investigation.

8. DIFFERENTIAL ROTATION

In this section we discuss the wind profiles induced by the thermal tide torque and estimate dissipation rates due to differential rotation.

The time-averaged force per unit volume on a fluid element due to the stellar tidal force acting on the thermal tide is

$$\mathbf{f}(\mathbf{x}) = -\langle \delta\rho \nabla U \rangle_t = \rho \langle \frac{\delta T}{T} \nabla U \rangle_t. \quad (76)$$

In the high frequency limit, for heating function $\delta\epsilon = \kappa_* F_* \exp(-\kappa_* y)$ we find a zonal component

$$f_\phi \simeq \rho n^2 R_p \frac{F_* \kappa_*}{(\Omega - n) C_p T} e^{-\kappa_* y}. \quad (77)$$

The ratio of the zonal acceleration $a_\phi = f_\phi / \rho$ on a fluid element to the planet's gravity is then

$$\begin{aligned} \frac{a_\phi}{g} &\sim \frac{n^2 R_p}{g} (\sigma t_{\text{th}})^{-1} \sim \frac{M_*}{M_p} \left(\frac{R_p}{a} \right)^3 (\sigma t_{\text{th}})^{-1} \\ &\sim 10^{-3} \left(\frac{M_*}{10^3 M_p} \right) \left(\frac{100 R_p}{a} \right)^3 (\sigma t_{\text{th}})^{-1}. \end{aligned} \quad (78)$$

In the absence of friction and Coriolis forces, the torqued layers would accelerate to the sound speed on a timescale of days. Coriolis forces will act to bend the zonal winds to produce circulation patterns with characteristic velocities $v_{\text{cir}} \sim a_\phi / \Omega \cos\theta$ sufficiently far from the equator. More importantly, the thermal tide force deposits net angular momentum. In the likely event that opposing gravitational tidal torques are exerted in a deeper layer, angular momentum transport is required to connect the source, due to the thermal tide, and the sink due to the gravitational tide.

As a simplest possible model, we ignore the Coriolis force and consider a turbulent boundary layer model (e.g. Landau & Lifshitz 1987) that is forced by the thermal and gravitational tidal torques. The thermal tide exerts

a stress

$$\begin{aligned} \tau &= \int dz f_\phi = \int dy n^2 R_p \frac{F_* \kappa_*}{(\Omega - n) C_p T} e^{-\kappa_* y} \\ &= n^2 R_p \frac{F_*}{(\Omega - n) C_p T} \end{aligned} \quad (79)$$

on the tidally forced layer. We treat this stress as applied in a thin layer at $z = z_1$, and the gravitational tide exerts an opposite stress at $z = z_2 < z_1$, deeper in the layer. The horizontal momentum equation for our toy model with horizontal velocity v and kinematic viscosity ν is

$$0 = \rho \nu \frac{d^2 v}{dz^2} + \tau \delta(z - z_1) - \tau \delta(z - z_2). \quad (80)$$

Setting the shear to be zero outside $z_2 \leq z \leq z_1$, we find the shear in between the two forced layers to be

$$\frac{dv}{dz} = \frac{\tau}{\rho \nu}. \quad (81)$$

Turbulent velocity fluctuations of size

$$\begin{aligned} v_* &\sim (\tau / \rho)^{1/2} = 40 \text{ m s}^{-1} \left(\frac{10^{-5} \text{ g cm}^{-3}}{\rho} \right)^{1/2} \\ &\times \left(\frac{n}{\Omega - n} \right)^{1/2} \left(\frac{R_p}{10^{10} \text{ cm}} \right)^{1/2} \left(\frac{4 \text{ days}}{P_{\text{orb}}} \right)^{3/2} \end{aligned} \quad (82)$$

transport momentum. We take a characteristic vertical distance of a scale height H , so that the viscosity $\nu \sim H v_*$. Eq.81 then becomes $dv/dz \sim v_*/H$. The shearing implies an energy dissipation rate

$$\begin{aligned} \dot{E}_{\text{shear}} &\sim 4\pi R_p^2 \int dz \rho \nu \left(\frac{dv}{dz} \right)^2 \sim 4\pi R_p^2 \rho \nu v_*^3 \\ &= 8 \times 10^{27} \text{ erg s}^{-1} \left(\frac{10^{-5} \text{ g cm}^{-3}}{\rho} \right)^{1/2} \\ &\times \left(\frac{n}{\Omega - n} \right)^{3/2} \left(\frac{R_p}{10^{10} \text{ cm}} \right)^{7/2} \left(\frac{4 \text{ days}}{P_{\text{orb}}} \right)^{9/2} \end{aligned} \quad (83)$$

This estimate for dissipation due to shearing is comparable to the dissipation rate of the gravitational tide in eq.62.

9. SUMMARY AND CONCLUSIONS

We investigated the role of thermal tides in short-orbital period gas giant exoplanets, the hot Jupiters. Our investigation consisted of two parts. We computed the time-dependent temperature and density perturbations in radiative atmospheres. We then applied these results for the thermal tide, and the Darwin-Hut theory of the gravitational tide, to compute spin, radius and eccentricity evolution.

Previous investigations (e.g. Ingersoll & Dobrovolskis 1978) for the case of Venus considered a shallow atmosphere bounded by ground at the base. In considering the thermal tide in hot Jupiters, we used radiative heat transport, and allowed incoming stellar radiation to be fully absorbed in the atmosphere. We computed the temperature perturbations in the atmosphere resulting from time-dependent insolation in order to estimate the induced thermal tide quadrupole moment. As

shown in the context of Venus, in the high frequency limit, the thermal tidal bulge *leads* the subsolar point (Ingersoll & Dobrovolskis 1978). In considering deep atmospheres, we include the effects of thermal diffusion, and found that the thermal tidal bulge still leads the substellar point for low tidal forcing frequencies, when heat can diffuse deep into the atmosphere. This result for the phase lead (for density, lag for temperature) is simplest to see in the results of nonlinear simulations in figures 2 - 5. Downward going diffusion waves at the base of the heated layer are discernible in figures 2 and 8 for the low frequency limit. The effective column and quadrupole moment are summarized in analytic formula in the high and low frequency limits in eq.41, 43, 49 and 50.

In appendix A, we derive the evolutionary equations for the planet's spin and orbit, as well as tidal heating rates for arbitrary quadrupole moments. These formula as used with the thermal tide quadrupole to compute equilibrium spin rates (§4), equilibrium tidal heating rates (§5), the growth/damping rate of eccentricity (§6), and simultaneous spin, orbital and thermal equilibrium (§7).

We find, contrary to the widely held assumption, that for reasonable heating depths and tidal Q , *hot Jupiters are far from a synchronous spin state* (see figure 10). At long orbital periods, the thermal tide torque dominates and the planet is highly asynchronous, while at smaller radii the gravitational tidal torque is larger, and the planet approaches a synchronous state. Direct measurements of the planetary rotation rate could confirm asynchronous rotation, although this appears difficult in the near future. Possible methods include detection of centrifugal flattening using high photometric precision transit observations (Seager & Hui 2002), and Doppler shifted absorption lines for transiting planets (Spiegel et al. 2007).

A more promising route to observationally constrain rotation rates at the moment may be through the indirect effect of planetary rotation on zonal winds, and the resulting change in phase of maximum thermal emission in Spitzer infrared observations. We have found, for uniform rotation, that flux perturbations are smaller in magnitude and have longer lag times in the high frequency limit than in the low frequency limit (see figure 4). The strength of zonal winds is expected to decrease for more rapid rotation rate as well (Showman et al. 2008). Hydrodynamic simulations of global circulation already contain the thermal tide quadrupole moment. "Turning on" the stellar tidal force in these simulations will torque the surface layer as described in §8, leading to spinup of the atmosphere, as well as momentum-driven circulation patterns in addition to the usual thermally-driven circulation. As argued by Goodman (2008), a source of dissipation such as that due to the gravitational tide or viscous friction is necessary to damp kinetic energy added to the atmosphere, and may affect steady-state wind speeds.

In §5, gravitational tidal dissipation due to asynchronous spin is shown to yield large *steady state* heat-

ing rates, sufficient in magnitude to power the large observed radii over the range $R_p = (1.2 - 1.8) \times R_J$ if the heat is deposited in the convective core. §8 shows that vertical shearing in the wind profiles between the layers torqued by the thermal and gravitational tides may also give heating rates large enough to alter the atmospheric temperature profiles, and perhaps slow the cooling of the planet (Bodenheimer et al. 2001).

In §6 we show that the thermal tide is capable of driving eccentricity. We compute the growth rate of eccentricity, in the limit of small eccentricity, finding narrow windows in orbital period in which the eccentricity is driven, while outside these windows it is even more strongly damped than for the gravitational tide alone. There are two consequences. As pointed out by Matsumura et al. (2008), a puzzle exists as to why *all* hot Jupiter orbits are not highly circular. It is observed that $\sim 25\%$ of hot Jupiters have eccentricities $e \geq 0.1$. Matsumura et al. (2008) argue that this must imply the planets with eccentric orbits have far larger Q than planets with circular orbits. Including the thermal tide, we find that it is expected that narrow windows in orbital period should exist in which eccentricity is driven to large values. This may explain the puzzling mix of zero and nonzero eccentricities in the observed planets. As a corollary, one cannot simply constrain the gravitational tidal Q , since its effects are mixed in with the thermal tide effect. In some ranges of orbital period they combine to cause more rapid circularization, while in other orbital period ranges they partially cancel. A more detailed study including both effects is required to place meaningful constraints on Q .

§7 shows that the timescales to achieve spin, orbital and thermal equilibrium are small or comparable to the Gyr ages of observed transiting planets. Simultaneous equilibria for spin period, radius and eccentricity are found. Radii increase strongly toward the star, mainly due to asynchronous spin, inside orbital periods of 1-2 weeks. Asynchronous spin again increases to longer orbital periods. Nonzero equilibrium values of eccentricity are found in the region where $e = 0$ is unstable.

In summary, this initial investigation has found that thermal tides have a significant impact on hot Jupiter rotation rates, eccentricities and thermal state, and that seemingly unrelated observation puzzles, such as large radii and nonzero eccentricities, may have a natural explanation within this model.

We thank Lars Bildsten, Peter Goldreich and Jonathan Mitchell for useful discussions. P.A. received support from an Alfred P. Sloan fellowship, and the Fund for Excellence in Science and Technology fellowship from the University of Virginia. A.S. acknowledges support from a Lyman Spitzer Jr. Fellowship given by Astrophysical Sciences at Princeton University as well as a Friends of the Institute Fellowship at the Institute for Advanced Study, in Princeton, NJ.

APPENDIX
SPIN, ORBIT AND THERMAL EVOLUTION RATES FOR ECCENTRIC ORBITS

The interaction Hamiltonian coupling the density field of the planet to the gravitational tidal potential of the star is given by

$$H = \int d^3x \rho(\mathbf{x}, t) U(\mathbf{x}, t) \quad (\text{A1})$$

where the integral is over the perturbed body of the planet, $\rho(\mathbf{x}, t)$ is the time-dependent density in the planet and $U(\mathbf{x}, t)$ the tidal potential. To evaluate this expression, we expand the tidal potential in spherical harmonics

$$U(\mathbf{x}, t) = -GM_\star \sum_{\ell m} \frac{4\pi}{2\ell + 1} \left(\frac{r^\ell}{D^{\ell+1}} \right) Y_{\ell m}^*(\pi/2, \Phi) Y_{\ell m}(\theta, \phi) \quad (\text{A2})$$

and define the time-dependent multipole moments of the planet

$$\mathcal{Q}_{\ell m}(t) = \int d^3x r^\ell Y_{\ell m}^*(\theta, \phi) \rho(\mathbf{x}, t). \quad (\text{A3})$$

Since $r^\ell \rho(\mathbf{x}, t)$ is a real quantity, and $Y_{\ell m}^* = (-1)^m Y_{\ell, -m}$, the moments must satisfy $\mathcal{Q}_{\ell m}^* = \mathcal{Q}_{\ell, -m}(-1)^m$. By defining $W_{\ell m} \equiv [4\pi/(2\ell + 1)] Y_{\ell m}(\pi/2, 0)$, the interaction Hamiltonian in eq.A1 may be conveniently expressed in terms of a sum over the tidal (spherical) harmonics

$$H(D, \Phi) = -GM_\star \sum_{\ell m} W_{\ell m} \mathcal{Q}_{\ell m}^*(t) \frac{e^{-im\Phi}}{D^{\ell+1}}. \quad (\text{A4})$$

The radial and tangential accelerations on the relative motion about the center of mass are then

$$a_D = -\frac{1}{\mu} \frac{\partial H}{\partial D} \quad (\text{A5})$$

$$a_\Phi = -\frac{1}{\mu D} \frac{\partial H}{\partial \Phi}, \quad (\text{A6})$$

where $\mu = M_p M_\star / (M_p + M_\star) \simeq M_p$ is the reduced mass. The change in orbital energy and angular momentum are then (Murray & Dermott 1999)

$$\dot{E}_{\text{orb}} = \mu \left(\dot{D} a_D + D \dot{\Phi} a_\Phi \right) \quad (\text{A7})$$

$$\dot{L}_{\text{orb}} = \mu D a_\Phi. \quad (\text{A8})$$

Since $E_{\text{orb}} = -GM_p M_\star / 2a$ and $L_{\text{orb}} = \mu \sqrt{G(M_p + M_\star) a (1 - e^2)}$, the changes in semi-major axis and eccentricity are

$$\frac{\dot{a}}{a} = \frac{2}{na\sqrt{1-e^2}} [e \sin \Phi a_D + (1 + e \cos \Phi) a_\Phi] \quad (\text{A9})$$

$$\frac{e\dot{e}}{1-e^2} = \frac{\dot{a}}{2a} - \frac{D a_\Phi}{na^2 \sqrt{1-e^2}}. \quad (\text{A10})$$

The torque on the planet is

$$N = - \int d^3x \rho(\mathbf{x}, t) \frac{\partial U(\mathbf{x}, t)}{\partial \phi} = \int d^3x \rho(\mathbf{x}, t) \frac{\partial U(\mathbf{x}, t)}{\partial \Phi} = -\dot{L}_{\text{orb}} \quad (\text{A11})$$

since the longitudes appear exclusively in the combination $\phi - \Phi$. This explicitly shows angular momentum is conserved over the orbit plus planet.

Given the quadrupole moments $\mathcal{Q}_{\ell m}(t)$, eq.A9, A10 and A11 can be integrated to find the changes in a , e and Ω . To isolate the secular evolution, we treat the orbit as Keplerian with elements a and e that vary on timescales much longer than the orbital period. We then expand all quantities in a Fourier series in time. Let

$$\left(\frac{a}{D} \right)^{\ell+1} e^{-im\Phi} = \sum_{k=-\infty}^{\infty} X_k^{\ell m}(e) e^{-iknt} \quad (\text{A12})$$

where the Hansen coefficients $X_k^{\ell m}(e)$ are defined as (Murray & Dermott 1999)

$$\begin{aligned} X_k^{\ell m}(e) &= \frac{n}{2\pi} \int_0^{2\pi/n} dt e^{iknt - im\Phi} \left(\frac{a}{D} \right)^{\ell+1} \\ &\simeq \delta_{mk} + \frac{e}{2} [(l+1+2m)\delta_{k,m+1} + (l+1-2m)\delta_{k,m-1}] + \mathcal{O}(e^2). \end{aligned} \quad (\text{A13})$$

The Hansen coefficients are real, and satisfy $X_{-k}^{\ell, -m} = X_k^{\ell m}$. The multipole moments are similarly expanded as

$$\mathcal{Q}_{\ell m}(t) = \sum_{k=-\infty}^{\infty} \mathcal{Q}_{\ell m k} e^{-iknt} \quad (\text{A14})$$

where

$$\mathcal{Q}_{\ell m k} = \frac{n}{2\pi} \int_0^{2\pi/n} dt e^{iknt} \mathcal{Q}_{\ell m}(t), \quad (\text{A15})$$

which satisfy $\mathcal{Q}_{\ell, -m, -k} = (-1)^m \mathcal{Q}_{\ell m k}^*$.

Plugging eq.A12 and A14 into eq. A9, A10 and A8, using the reality conditions relating (m, k) to $(-m, -k)$, and and isolating the secular terms, we find

$$\frac{\dot{a}}{a} = \frac{\dot{E}_{\text{orb}}}{|E_{\text{orb}}|} = n \sum_{\ell m k} W_{\ell m} X_k^{\ell m} \left(\frac{\text{Im}(\mathcal{Q}_{\ell m k})}{M_p a^\ell} \right) (-2k) \quad (\text{A16})$$

$$\frac{e\dot{e}}{\sqrt{1-e^2}} = n \sum_{\ell m k} W_{\ell m} X_k^{\ell m} \left(\frac{\text{Im}(\mathcal{Q}_{\ell m k})}{M_p a^\ell} \right) (m - k\sqrt{1-e^2}) \quad (\text{A17})$$

$$N = -\dot{L}_{\text{orb}} = \mu n^2 a^2 \sum_{\ell m k} W_{\ell m} X_k^{\ell m} \left(\frac{\text{Im}(\mathcal{Q}_{\ell m k})}{M_p a^\ell} \right) (m). \quad (\text{A18})$$

The change in spin energy of the planet is

$$\dot{E}_{\text{spin}} = \Omega N = \mu n^2 a^2 \Omega \sum_{\ell m k} W_{\ell m} X_k^{\ell m} \left(\frac{\text{Im}(\mathcal{Q}_{\ell m k})}{M_p a^\ell} \right) (m). \quad (\text{A19})$$

The energy change in the orbit and spin is given by

$$\dot{E}_{\text{orb}} + \dot{E}_{\text{spin}} = -\mu n^2 a^2 \sum_{\ell m k} W_{\ell m} X_k^{\ell m} \left(\frac{\text{Im}(\mathcal{Q}_{\ell m k})}{M_p a^\ell} \right) (kn - m\Omega). \quad (\text{A20})$$

Here $\sigma_{km} = kn - m\Omega$ is the forcing frequency in the frame corotating with the planet.

In the case of gravitational tides whose phase lag is due to dissipation, energy is taken out of the spin or orbit and deposited as heat in the planet, so $\dot{E}_{\text{orb}} + \dot{E}_{\text{spin}} < 0$. In this case we define the heating rate of the planet as

$$\dot{E}_{\text{heat}}^{(\text{GT})} = -\left(\dot{E}_{\text{orb}} + \dot{E}_{\text{spin}}\right)^{\text{GT}} = \mu n^2 a^2 \sum_{\ell m k} W_{\ell m} X_k^{\ell m} \left(\frac{\text{Im}(\mathcal{Q}_{\ell m k}^{(\text{GT})})}{M_p a^\ell} \right) (kn - m\Omega) \quad (\text{A21})$$

This heating rate will be used for the thermal evolution of the planet. In the case of the thermal tide, work was needed to move the fluid against the stellar tidal force, so that $\dot{E}_{\text{orb}} + \dot{E}_{\text{spin}} > 0$. Ultimately this energy is derived from the stellar radiation field. In this case we define the rate of work done on the atmosphere due to heating from insolation as

$$\dot{E}_{\text{work}}^{(\text{TT})} = \left(\dot{E}_{\text{orb}} + \dot{E}_{\text{spin}}\right)^{\text{TT}} = -\mu n^2 a^2 \sum_{\ell m k} W_{\ell m} X_k^{\ell m} \left(\frac{\text{Im}(\mathcal{Q}_{\ell m k}^{(\text{TT})})}{M_p a^\ell} \right) (kn - m\Omega). \quad (\text{A22})$$

Since we do not include zonal motions in the equations solved in this paper, we cannot explicitly compute this work done against gravity. Our assumption is that the constant pressure approximation adequately represents the physics of heating by insolation. We will include fluid motions and compute this work in a future investigation.

In equilibrium, the work done on the atmosphere first goes into spin or orbital energy, and then is dissipated as heat in the planet. Before equilibrium is reached, energy can be either lost or gained from the spin and orbit.

The secular equations depend on the component of the quadrupole moments out of phase with the tidal acceleration, hence the imaginary components are required in the eq.A16, A17 and A18. While we perform the sums over ℓ , m and k until convergence is achieved for our numerical work, it is useful to have analytic limits to compare to. The torque on the planet for a circular orbit is dominated by the semi-diurnal term with $|m| = 2$ and forcing frequency $2(n - \Omega)$. The torque at this order is

$$N = 4 \left(\frac{3\pi}{10} \right)^{1/2} \left(\frac{M_p + M_\star}{M_\star} \right) n^2 \text{Im}(\mathcal{Q}_{222}). \quad (\text{A23})$$

The sign in eq.A23 is such that density perturbations *leading* the heating tend to torque the planet *away* from synchronous rotation, and vice versa. A schematic drawing for the relevant semi-diurnal tide ($m = 2$) is shown in fig. 1.

At lowest order in e , the circularization rate is dominated by the $m = 0$ harmonic with frequency n , as well as the $|m| = 2$ harmonics with frequencies $2(n - \Omega)$, $3n - 2\Omega$, and $n - 2\Omega$. The circularization rate to lowest order in e is

$$\dot{e} = \sqrt{\frac{\pi}{5}} \frac{n}{M_p a^2} \left[\sqrt{6}e \operatorname{Im}(\mathcal{Q}_{222}) + 3 \operatorname{Im}(\mathcal{Q}_{201}) - 7\sqrt{\frac{3}{2}} \operatorname{Im}(\mathcal{Q}_{223}) - \sqrt{\frac{3}{2}} \operatorname{Im}(\mathcal{Q}_{221}) \right]. \quad (\text{A24})$$

Eccentricity may be either driven or damped depending on the relative sizes and signs of each term.

MASS-RADIUS RELATION AND CORE COOLING LUMINOSITY

Our model consists of an adiabatic interior connected to the “background” atmosphere structure described in §3.5. We do not include a solid core at the center, which would decrease the radius.

For the adiabatic interior we solve

$$\frac{dm}{dr} = 4\pi r^2 \rho \quad (\text{B1})$$

$$\frac{dP}{dr} = -\frac{Gm\rho}{r^2} \quad (\text{B2})$$

$$S(P, T) = S_{\text{core}} = \text{constant}. \quad (\text{B3})$$

We use the equation of state from Saumon et al. (1995) with 70% hydrogen and 30% helium by mass. Given the core entropy S_{core} and central pressure P_c , the equations are integrated out to a reference pressure $P_{\text{ref}} = 10^4 \text{ dyne cm}^{-2}$, yielding a mass M_p , radius R_p , and surface gravity $g = GM_p/R_p^2$. Note that the computed radii are at the fiducial pressure, not the self-consistent radius at the optical or infrared photosphere including transit geometry effects. The error in the radius will be of order a few scale heights, which amounts to of order a percent of the planetary radius.

Given the solution for the adiabatic core, we integrate eq.29 and 30 inward from the top of the atmosphere. In addition to “given” parameters $F_*(a)$, e , θ and κ_* , a guess for F_{core} must be chosen. We integrate inward until the Schwarzschild criterion is violated, yielding the entropy of the radiative atmosphere, S_{atm} , at the radiative-convective boundary. In order that the radiative atmosphere matches smoothly onto the adiabatic interior, we adjust F_{core} until $S_{\text{atm}} = S_{\text{core}}$. This yields the “background” radiative atmosphere, T versus P , used to find the perturbations in §3.5. The cooling luminosity of the core is found by integrating F_{core} over latitude

$$L_{\text{core}} = 2\pi R_p^2 \int_0^\pi d\theta \sin\theta F_{\text{core}}(\theta). \quad (\text{B4})$$

An example of L_{core} is given in figure 11.

This model for the mass-radius relation and cooling luminosity is a modified version Arras & Bildsten (2006). Their upper boundary condition assumed the existence of an isothermal region just below where the stellar radiation is absorbed. They assigned this region the temperature T_{deep} , and treated this as a parameter of the model. Here we improve on Arras & Bildsten (2006) by calculating, rather than parametrizing, the temperature at the atmosphere.

REFERENCES

- Allard, F., Hauschildt, P. H., Alexander, D. R., Tamanai, A., & Schweitzer, A. 2001, *ApJ*, 556, 357
- Arras, P., & Bildsten, L. 2006, *ApJ*, 650, 394
- Bender, C. M., & Orszag, S. A. 1978, *Advanced Mathematical Methods for Scientists and Engineers*, New York: McGraw-Hill, 1978,
- Bodenheimer, P., Lin, D. N. C., & Mardling, R. A. 2001, *ApJ*, 548, 466
- Burrows, A., Guillot, T., Hubbard, W. B., Marley, M. S., Saumon, D., Lunine, J. I., & Sudarsky, D. 2000, *ApJ*, 534, L97
- Darwin, G. H. 1879, *The Observatory*, 3, 79
- Dobbs-Dixon, I., Lin, D. N. C., & Mardling, R. A. 2004, *ApJ*, 610, 464
- Dobrovolskis, A. R., & Ingersoll, A. P. 1980, *Icarus*, 41, 1
- Fortney, J. J., Lodders, K., Marley, M. S., & Freedman, R. S. 2008, *ApJ*, 678, 1419
- Fortney, J. J. 2008, arXiv:0801.4943
- Gold, T., & Soter, S. 1969, *Icarus*, 11, 356
- Goldreich, P., & Nicholson, P. D. 1977, *Icarus*, 30, 301
- Goldreich, P., & Soter, S. 1966, *Icarus*, 5, 375
- Goodman, J. 2008, arXiv:0810.1282
- Goodman, J., & Lackner, C. 2008, arXiv:0812.1028
- Landau, L.D., & Lifshitz, E.M. 1987, *Fluid Mechanics*, 2nd Edition, New York: Pergamon Press
- Laughlin, G., Marcy, G. W., Vogt, S. S., Fischer, D. A., & Butler, R. P. 2005, *ApJ*, 629, L121
- Liou, K. N. 2002, *An Introduction to Atmospheric Radiation* (vol.2), Academic Press, Amsterdam.
- Mardling, R. A., & Lin, D. N. C. 2002, *ApJ*, 573, 829
- Matsumura, S., Takeda, G., & Rasio, F. 2008, ArXiv e-prints, 808, arXiv:0808.3724
- Hubeny, I., Burrows, A., & Sudarsky, D. 2003, *ApJ*, 594, 1011
- Hut, P. 1981, *A&A*, 99, 126
- Ingersoll, A. P., & Dobrovolskis, A. R. 1978, *Nature*, 275, 37
- Jackson, B., Greenberg, R., & Barnes, R. 2008, *ApJ*, 678, 1396
- Levermore, C. D., & Pomraning, G. C. 1981, *ApJ*, 248, 321
- Marcy, G. W., Butler, R. P., Williams, E., Bildsten, L., Graham, J. R., Ghez, A. M., & Jernigan, J. G. 1997, *ApJ*, 481, 926
- Matsumura, S., Takeda, G., & Rasio, F. A. 2008, *ApJ*, 686, L29
- Murray, C. D., & Dermott, S. F. 1999, *Solar system dynamics by Murray, C. D., 1999,*
- Ogilvie, G. I., & Lin, D. N. C. 2004, *ApJ*, 610, 477
- Piro, A. L., Arras, P., & Bildsten, L. 2005, *ApJ*, 628, 401
- Rasio, F. A., Tout, C. A., Lubow, S. H., & Livio, M. 1996, *ApJ*, 470, 1187
- Saumon, D., Chabrier, G., & van Horn, H. M. 1995, *ApJS*, 99, 713
- Seager, S., & Hui, L. 2002, *ApJ*, 574, 1004
- Showman, A. P., Fortney, J. J., Lian, Y., Marley, M. S., Freedman, R. S., Knutson, H. A., & Charbonneau, D. 2008, arXiv:0809.2089
- Spiegel, D. S., Haiman, Z., & Gaudi, B. S. 2007, *ApJ*, 669, 1324
- Yoder, C. F., & Peale, S. J. 1981, *Icarus*, 47, 1
- Wu, Y. 2005, *ApJ*, 635, 688